fractal and fractional

MDPI

Article

A Unified Comparative Framework for Fractional-Order Operator Approximation with Pareto-Based Analysis

Abebe Alemu Wendimu *, Radek Matušů, Ibrahim Shaikh, Mihret Kochito Wolde, Meron Tadele Roba and Feleke Tsegaye Yareshe

Department of Automation and Control Engineering, Faculty of Applied Informatics, Tomas Bata University in Zlín, nám. T. G. Masaryka 5555, 760 01 Zlín, Czech Republic; rmatusu@utb.cz (R.M.); shaikh@utb.cz (I.S.); wolde@utb.cz (M.K.W.); roba@utb.cz (M.T.R.); yareshe@utb.cz (F.T.Y.)

* Correspondence: a_wendimu@utb.cz

Abstract

Fractional-order operators play a fundamental role in the modeling and control of complex dynamical systems; however, their infinite-dimensional nature necessitates rational approximation for practical implementation. This paper presents a unified comparative framework for evaluating widely used approximation methods, including standard and refined Oustaloup filters, continued fraction expansion (CFE), Matsuda, curve-fitting, and modified stability boundary locus (M-SBL) approaches. A systematic evaluation methodology is developed to assess these methods based on frequency-domain accuracy, time-domain performance, and robustness. Furthermore, a Pareto-based multi-objective analysis is introduced to explicitly capture the trade-offs among conflicting performance criteria, enabling the identification of non-dominated solutions without relying on weighted-sum formulations. Extensive simulations are conducted over a wide frequency range to evaluate approximation accuracy and control-oriented performance. The results reveal that different methods exhibit distinct trade-offs between accuracy, robustness, and complexity. In particular, the Oustaloup and M-SBL approaches demonstrate strong overall performance across multiple criteria, while methods such as CFE and curve-fitting show limitations under wide-band conditions. The proposed framework provides a systematic and reproducible basis for selecting appropriate approximation techniques in fractional-order control applications, offering valuable insights into their practical implementation and performance trade-offs.

Keywords: fractional-order calculus; fractional-order operators; approximation methods; Oustaloup filter; continued fraction expansion; Matsuda method; curve fitting; M-SBL; multi-objective optimization; Pareto analysis; control systems

Check for updates

Academic Editor: António Lopes

Received: 12 April 2026
Revised: 30 April 2026
Accepted: 7 May 2026
Published: 9 May 2026

Copyright: © 2026 by the authors. Licensee MDPI, Basel, Switzerland. This article is an open access article distributed under the terms and conditions of the Creative Commons Attribution (CC BY) license.

1. Introduction

Fractional-order calculus (FOC) has emerged as a powerful mathematical framework for modeling and control of dynamical systems, offering enhanced flexibility compared to conventional integer-order approaches [1,2]. By extending differentiation and integration to non-integer orders, it enables the representation of memory and hereditary effects that are inherently present in many physical, biological, and engineering processes [3,4]. This capability constitutes a key advantage over classical models, which typically assume local and instantaneous behavior, thereby limiting their ability to describe complex dynamics accurately. As a result, fractional-order models provide improved accuracy and realism, particularly for systems with long-term dependencies and nonlocal interactions.

Due to these advantages, fractional-order calculus has been widely applied across multiple disciplines. In control engineering, it is extensively used in fractional-order PID controllers to enhance robustness and tuning flexibility [1,5]. In bioengineering, it effectively models viscoelastic tissues and diffusion processes [3,4], while in electrical engineering, it accurately represents non-ideal components such as supercapacitors and constant phase elements [6,7]. Furthermore, it is applied in mechanical systems for viscoelastic modeling and vibration analysis [8], in fluid dynamics for anomalous diffusion [2], and in robotics and energy systems for improving control performance and dynamic modeling [9–11]. Overall, FOC provides a unified and effective framework for modeling complex systems where classical integer-order approaches are insufficient.

Despite these promising applications and advantages, the practical realization of fractional operators such as s^{α} and $\frac{1}{s^{\alpha}}$ remains a central challenge in system modeling, identification, and control. Unlike integer-order operators, fractional operators lack direct physical interpretation and straightforward numerical implementation. Consequently, their realization depends on approximation techniques that reproduce their behavior over a specified frequency range. Rational approximation of fractional operators is therefore essential for practical applications. The accuracy of these approximations has a direct impact on model accuracy, controller performance, and system stability, making the selection of an appropriate approximation method a critical step in fractional-order system design. In the literature, a variety of approximation techniques have been proposed to represent fractional-order operators using finite-dimensional models. One of the most widely used approaches is the Oustaloup recursive approximation, introduced for approximating fractional operators over a specified frequency band [7]. Refined variants of the Oustaloup have been developed to improve accuracy, particularly near the edge of the band, and are widely used in practical control implementations [9]. Alternative approaches include continued fraction expansion (CFE), which provides low-order rational approximations with simple structures [12], and Matsuda's method, which constructs approximations based on interpolation of frequency response data [13]. The Carlson method and Charef method offer simple formulations but are generally limited to narrowband applications [6,14]. Curve-fitting approaches, including frequency-domain identification techniques such as the Sanathanan–Koerner algorithm, provide flexible data-driven approximations that can closely match measured responses [15,16]. More recently, stability-oriented techniques such as the modified stability boundary locus (M-SBL) method have been introduced to incorporate stability considerations directly into the approximation process [17,18]. Several studies have compared these methods primarily in terms of frequency-domain accuracy, often focusing on magnitude and phase errors within a predefined frequency band. However, the existing literature reveals several important limitations. First, most works emphasize accuracy improvement without systematically analyzing the trade-off between approximation fidelity and computational complexity. Second, robustness with respect to variations in the design frequency band is rarely addressed, even though practical applications often involve uncertain or varying operating ranges. Third, stability preservation and numerical conditioning, which are critical for implementation in control systems, are often treated only implicitly or not evaluated quantitatively. Finally, there is a lack of a unified decision-making framework that integrates multiple performance criteria and supports the selection of the most suitable approximation method for a given application.

These limitations indicate that although there are numerous approximation methods, a comprehensive and structured comparative analysis that jointly considers accuracy, robustness, complexity, stability, and numerical behavior is still lacking.

To address these gaps, this paper presents a comprehensive comparative study of fractional-order approximation methods supported by a unified evaluation framework.

The main objective is to systematically analyze widely used approximation techniques, considering multiple performance criteria, including frequency-domain accuracy, time-domain behavior, computational complexity, robustness to frequency-band variation, stability, and numerical conditioning. In addition to conventional error analysis, this work introduces a Pareto-based multi-objective decision framework to identify optimal trade-offs among competing criteria. This approach enables a structured comparison of approximation methods and provides practical guidance for selecting the most appropriate method based on specific design requirements. The central research question addressed in this study is how to systematically evaluate and select fractional-order approximation methods by jointly considering accuracy, robustness, computational complexity, stability, and numerical implementation aspects. To address this question, this article develops a unified analytical and comparative framework that integrates both theoretical characterization and practical performance evaluation. This framework provides a structured basis for understanding the trade-offs inherent in fractional-order approximation and supports informed method selection for engineering applications.

The main contributions of this study are summarized as follows:

- A unified formulation and critical review of major fractional-order approximation methods, highlighting their underlying mathematical structures.
- The development of a comprehensive evaluation framework that incorporates frequency-domain accuracy, time-domain performance, computational complexity, robustness to frequency-band variation, stability, and numerical conditioning.
- A Pareto-based multi-objective decision framework for systematic selection of approximation methods based on application-specific requirements.

By bridging theoretical analysis with practical validation, this study provides a coherent guideline for the selection and implementation of fractional-order approximation methods, particularly in control applications where accuracy, robustness, and computational efficiency must be simultaneously satisfied.

Following this introduction, the remainder of the paper is structured as follows. Section 2 presents the mathematical foundations of fractional-order calculus and formulates the problem. Section 3 introduces the considered fractional-order operator approximation methods along with the corresponding analytical framework. Section 4 details the proposed comparative evaluation framework and methodology. Section 5 presents and discusses the obtained results. Section 6 provides an illustrative example demonstrating the application of the considered approximation methods. Finally, Section 7 concludes the paper by summarizing the main findings, highlighting practical implications, and outlining directions for future research.

2. Mathematical Preliminaries and Problem Formulation

This section establishes the theoretical foundation required for fractional-order system modeling, approximation, and control design by introducing the fundamental concepts of fractional calculus, system representations, and a unified formulation of the approximation problem, which is essential for subsequent comparative analysis.

2.1. Fundamentals of Fractional Calculus

Fractional calculus extends the classical concepts of differentiation and integration to non-integer orders, thereby providing a generalized mathematical framework capable of describing systems with memory and hereditary characteristics. The general fractional operator is defined as

$$ {}_aD_t^{\alpha} f(t) = \begin{cases} \dfrac{d^{\alpha}}{dt^{\alpha}} f(t), & \text{if } \Re(\alpha) > 0, \\ f(t), & \text{if } \Re(\alpha) = 0, \\ \dfrac{1}{\Gamma(-\alpha)} \displaystyle\int_a^t (t-\tau)^{-\alpha-1} f(\tau)\, d\tau, & \text{if } \Re(\alpha) < 0, \end{cases} \tag{1} $$

where $\alpha \in \mathbb{R}$ (or $\mathbb{C}$), and $\Gamma(\cdot)$ denotes the Gamma function. This formulation reduces to classical operators for integer values, ensuring consistency with conventional calculus. An equivalent and widely used time-domain definition is the Grünwald–Letnikov (G–L) fractional derivative, which provides a limit-based representation of the same operator. It is defined as

$$ {}_a^{GL}D_t^{\alpha} f(t) = \lim_{h \to 0} \frac{1}{h^{\alpha}} \sum_{k=0}^{\left\lfloor \frac{t-a}{h} \right\rfloor} (-1)^k \binom{\alpha}{k} f(t-kh), \tag{2} $$

where $\binom{\alpha}{k}$ denotes the generalized binomial coefficient given by

$$ \binom{\alpha}{k} = \frac{\Gamma(\alpha+1)}{\Gamma(k+1)\,\Gamma(\alpha-k+1)}, $$

where Gamma function is defined as

$$ \Gamma(x) = \int_0^{\infty} t^{x-1} e^{-t}\, dt, \quad x > 0. \tag{3} $$

The Grünwald–Letnikov formulation is particularly suitable for numerical implementation, while the integral form in (1) provides analytical insight into the memory effect inherent in fractional-order systems. Although fractional calculus can be extended to complex-order operators [7,11,19–24], this study focuses on real-valued orders due to their direct relevance in engineering applications. Since the operator ${}_aD_t^{\alpha}$ is inherently infinite-dimensional, practical realization typically relies on approximation techniques, often implemented in the frequency domain using rational transfer functions [25].

2.2. Fractional-Order System Representation

A linear time-invariant fractional-order system can be expressed using fractional differential equations of the form

$$ \sum_{i=0}^{n} a_i D^{\alpha_i} y(t) = \sum_{j=0}^{m} b_j D^{\beta_j} u(t), \tag{4} $$

where $y(t)$ and $u(t)$ represent the system output and input, respectively, and the derivative orders α_i and β_j are real positive numbers. By applying the Laplace transform under zero initial conditions, fractional derivatives are mapped into algebraic expressions as $D^{\alpha} \to s^{\alpha}$, leading to

$$ \sum_{i=0}^{n} a_i s^{\alpha_i} Y(s) = \sum_{j=0}^{m} b_j s^{\beta_j} U(s), \tag{5} $$

from which the transfer function representation is obtained as

$$ G(s) = \frac{Y(s)}{U(s)} = \frac{\sum_{j=0}^{m} b_j s^{\beta_j}}{\sum_{i=0}^{n} a_i s^{\alpha_i}}. \tag{6} $$

2.2.1. Commensurate Fractional-Order Systems

For commensurate systems characterized by a common base order γ, the transfer function can be rewritten as

$$G(s) = \frac{b_m s^{m\gamma} + \cdots + b_0}{a_n s^{n\gamma} + \cdots + a_0}, \tag{7}$$

which simplifies numerical implementation and facilitates system identification.

2.2.2. Stability Mapping Between Integer-Order and Fractional-Order Systems

If an integer-order characteristic polynomial is written as

$$P(s) = a_n s^n + a_{n-1} s^{n-1} + \cdots + a_1 s + a_0, \tag{8}$$

then its fractional-order counterpart is obtained by replacing s with s^α, yielding

$$P(s^\alpha) = a_n s^{n\alpha} + a_{n-1} s^{(n-1)\alpha} + \cdots + a_1 s^\alpha + a_0. \tag{9}$$

By introducing the transformation $\lambda = s^\alpha$, the characteristic equation can be rewritten as

$$a_n \lambda^n + a_{n-1} \lambda^{n-1} + \cdots + a_1 \lambda + a_0 = 0.$$

The roots of this polynomial in the λ-plane must satisfy [26]

$$|\arg(\lambda_i)| > \frac{\alpha\pi}{2}$$

to ensure asymptotic stability of the fractional-order system. In contrast, the stability condition for integer-order systems is given by

$$\Re(s_i) < 0.$$

Therefore, the mapping from integer-order to fractional-order stability can be expressed as

$$\Re(s_i) < 0 \quad \Longrightarrow \quad |\arg(\lambda_i)| > \frac{\alpha\pi}{2}, \qquad \lambda = s^\alpha. \tag{10}$$

This transformation shows that the classical left half-plane stability region is generalized into a sector-shaped region in the fractional-order case, where stability depends on the angular location of the poles rather than solely on their real parts. Figure 1 illustrates the stability regions for integer-order and fractional-order systems. Thus, stability is evaluated based on the pole locations, where a model is considered stable if all poles satisfy the above-mentioned rules [27].

2.3. Fractional-Order PID Controller

The fractional-order PID (FOPID) controller extends the classical PID structure by introducing fractional powers of the integral and derivative terms, which can be expressed as

$$G_c(s) = K_p + \frac{K_i}{s^\lambda} + K_d s^\mu, \tag{11}$$

where K_p, K_i, and K_d are controller gains, and $\lambda, \mu \in (0, 1]$ denote the fractional orders. The inclusion of these additional tuning parameters provides enhanced flexibility in shaping system dynamics.

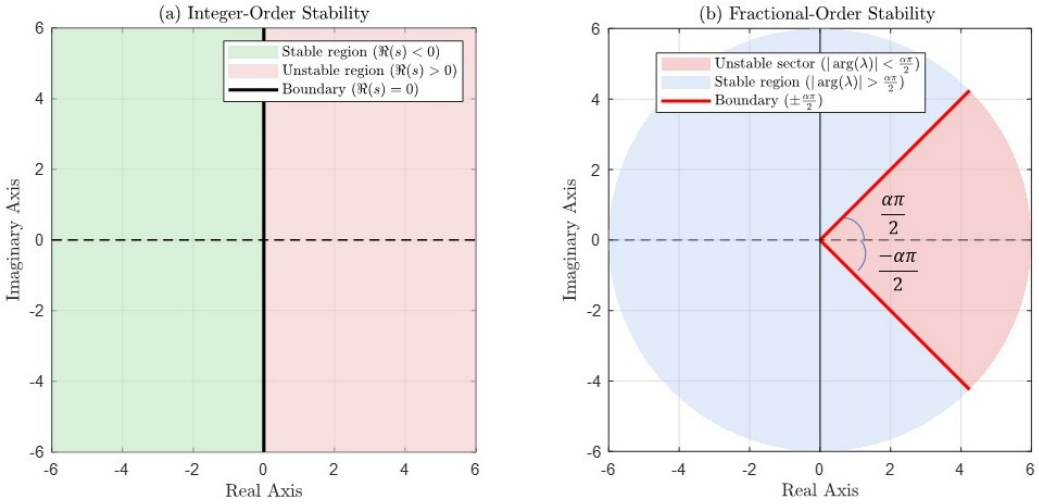


Figure 1. Comparison of stability regions for integer-order and fractional-order systems. (**a**) The integer-order system is stable in the left half-plane defined by $\Re(s) < 0$, with the imaginary axis representing the stability boundary. (**b**) The fractional-order system exhibits a sector-shaped stability region, where instability is confined to $|\arg(\lambda)| < \frac{\alpha\pi}{2}$ and stability is achieved outside this sector. This illustrates the transformation of the classical half−plane stability condition into an angle-dependent criterion. For $\alpha = 1$, the fractional−order system reduces to the classical integer-order case, and therefore, the stability regions of (**a**) and (**b**) coincide.

2.4. Problem Formulation

From the above formulations, it is evident that fractional-order modeling and control fundamentally depend on operators of the form s^{α} and $s^{-\alpha}$, which are non-rational and therefore cannot be directly implemented in physical or digital systems. Consequently, the core problem addressed in this study is to construct a finite-dimensional rational approximation of the form

$$G_{\text{apx}}(s) = \frac{P(s)}{Q(s)} = \frac{\sum_{k=0}^{n} a_k s^k}{\sum_{k=0}^{n} b_k s^k}, \tag{12}$$

such that

$$G_{\text{apx}}(j\omega) \approx G(j\omega), \quad \forall \omega \in [\omega_L, \omega_H], \tag{13}$$

where $[\omega_L, \omega_H]$ represents the design frequency band.

The frequency response of the fractional operator is given by

$$G(j\omega) = (j\omega)^{\alpha} = \omega^{\alpha}\left[\cos\left(\frac{\alpha\pi}{2}\right) + j\sin\left(\frac{\alpha\pi}{2}\right)\right],$$

which exhibits a constant phase shift of

$$\angle G(j\omega) = \frac{\alpha\pi}{2}$$

and a magnitude slope of 20α dB/decade.

2.5. Performance Metrics

To enable systematic evaluation of approximation methods, a unified set of performance metrics is defined.

Frequency-domain accuracy is quantified using magnitude and phase errors:

$$e_m(\omega_k) = 20\log_{10}|G_{\text{apx}}(j\omega_k)| - 20\log_{10}|G(j\omega_k)|, \tag{14}$$

$$e_p(\omega_k) = \angle G_{\text{apx}}(j\omega_k) - \angle G(j\omega_k), \tag{15}$$

from which the root-mean-square errors are computed as

$$\mathrm{RMSE}_m = \sqrt{\frac{1}{N}\sum_{k=1}^{N} e_m^2(\omega_k)}, \tag{16}$$

$$\mathrm{RMSE}_p = \sqrt{\frac{1}{N}\sum_{k=1}^{N} e_p^2(\omega_k)}, \tag{17}$$

while the maximum deviations are defined as

$$\mathrm{Max}_m = \max_k |e_m(\omega_k)|, \tag{18}$$

$$\mathrm{Max}_p = \max_k |e_p(\omega_k)|. \tag{19}$$

Time-domain performance is evaluated using the error signal $e(t) = y(t) - y_{\mathrm{apx}}(t)$, where the integral absolute error and integral squared error are given by

$$\mathrm{IAE} = \int_0^T |e(t)|dt, \tag{20}$$

$$\mathrm{ISE} = \int_0^T e^2(t)dt. \tag{21}$$

Computational complexity is characterized by model order, defined by the number of poles and zeros, as well as computational time required for model construction and simulation.

2.6. Remarks on Approximation Characteristics

The approximation error is inherently dependent on the selected frequency band, because most methods place poles and zeros within the design interval, yielding optimal accuracy within the band and degrading outside it. Furthermore, the approximation problem is intrinsically multi-objective, requiring a balance between accuracy, computational complexity, robustness, and numerical stability. The performance metrics defined in this section provide a consistent and unified basis for comparing different approximation methods throughout this study.

3. Fractional-Order Approximation Methods

This section introduces the main approximation techniques considered in this study. In each case, the objective is to approximate the fractional-order operator $G(s) = s^\alpha$ by means of a finite-dimensional rational transfer function that preserves the essential frequency-domain characteristics of the ideal operator within a prescribed frequency interval $[\omega_L, \omega_H]$.

3.1. Oustaloup Recursive Approximation (ORA)

The Oustaloup recursive approximation (ORA) is one of the most widely used frequency-domain methods for approximating fractional-order operators [9,12,22,28]. Its main idea is to represent s^α as a rational transfer function obtained by recursively distributing poles and zeros on a logarithmic scale within the selected frequency band. This construction provides good approximation accuracy within the design interval and has therefore become a standard choice in fractional-order control applications.

The ORA model is written as

$$G_{\mathrm{ORA}}(s) = K \prod_{k=-N}^{N} \frac{s+\omega_k'}{s+\omega_k}, \tag{22}$$

where N denotes the approximation order, ω_k and ω_k' are the pole and zero frequencies, respectively, and K is a gain term introduced to preserve the correct scaling. The poles and zeros are defined as

$$\omega_k = \omega_L \left(\frac{\omega_H}{\omega_L}\right)^{\frac{k+N+\frac{1+\alpha}{2}}{2N+1}}, \tag{23}$$

$$\omega_k' = \omega_L \left(\frac{\omega_H}{\omega_L}\right)^{\frac{k+N+\frac{1-\alpha}{2}}{2N+1}}, \tag{24}$$

while the gain is given by

$$K = \omega_H^{\alpha}. \tag{25}$$

An important structural property of ORA is that an approximation of order N produces a rational model with $2N+1$ poles and $2N+1$ zeros. In other words, the structural complexity increases linearly with the approximation order, which improves approximation flexibility but also raises implementation cost. The behavior of ORA for different approximation orders is illustrated in Figure 2, which compares the Bode magnitude and phase responses of the exact operator $s^{0.5}$ with third-, fifth-, and eighth-order ORA models over the frequency band $[10^{-3}, 10^{3}]$ rad/s. The results show that the approximation becomes less sensitive to further order increases once $N \geq 5$. For the lower-order case $N = 3$, visible ripples appear in both magnitude and phase responses, whereas higher orders reduce these oscillations and produce smoother frequency characteristics.

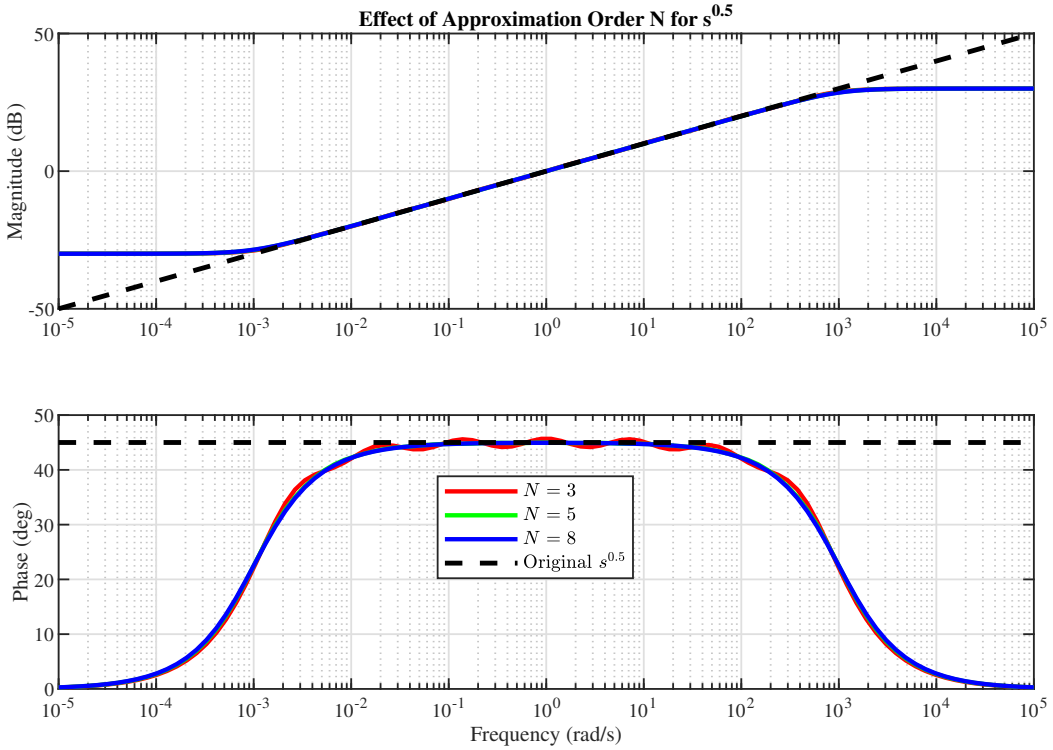


Figure 2. Bode magnitude and phase responses of the third-, fifth-, and eighth-order Oustaloup recursive approximation (ORA) models of $s^{0.5}$ over the frequency band $[10^{-3}, 10^{3}]$ rad/s.

This trend is also reflected in Table 1, where increasing the order from $N = 3$ to $N = 8$ leads to only minor changes in RMSE and maximum error values, indicating that the ORA exhibits weak order sensitivity beyond moderate approximation orders. The influence of the design frequency band is shown in Figure 3 and Table 2. In contrast to the relatively small effect of increasing N, the selected frequency interval has a much stronger impact on approximation quality. The widest band produces the lowest overall errors, whereas narrower bands lead to larger magnitude and phase deviations together with increased time-domain error indices.

Table 1. Frequency- and time-domain performance comparison of third-, fifth-, and eighth-order ORA and ROA models of $s^{0.5}$ over the frequency band $[10^{-3}, 10^{3}]$ rad/s.

N	RMSE_m (dB)		RMSE_p (deg)		Max_m (dB)		Max_p (deg)		IAE		ISE	
	ORA	ROA	ORA	ROA	ORA	ROA	ORA	ROA	ORA	ROA	ORA	ROA
3	7.3486	4.3375	25.939	21.006	20	14.439	44.745	44.109	0.10501	0.40243	0.63739	5.9320
5	7.3549	4.3374	25.828	20.996	20	14.439	44.727	44.091	0.09153	0.38693	0.63805	5.9314
8	7.3579	4.3378	25.789	20.995	20	14.439	44.719	44.083	0.09216	0.38651	0.63824	5.9314

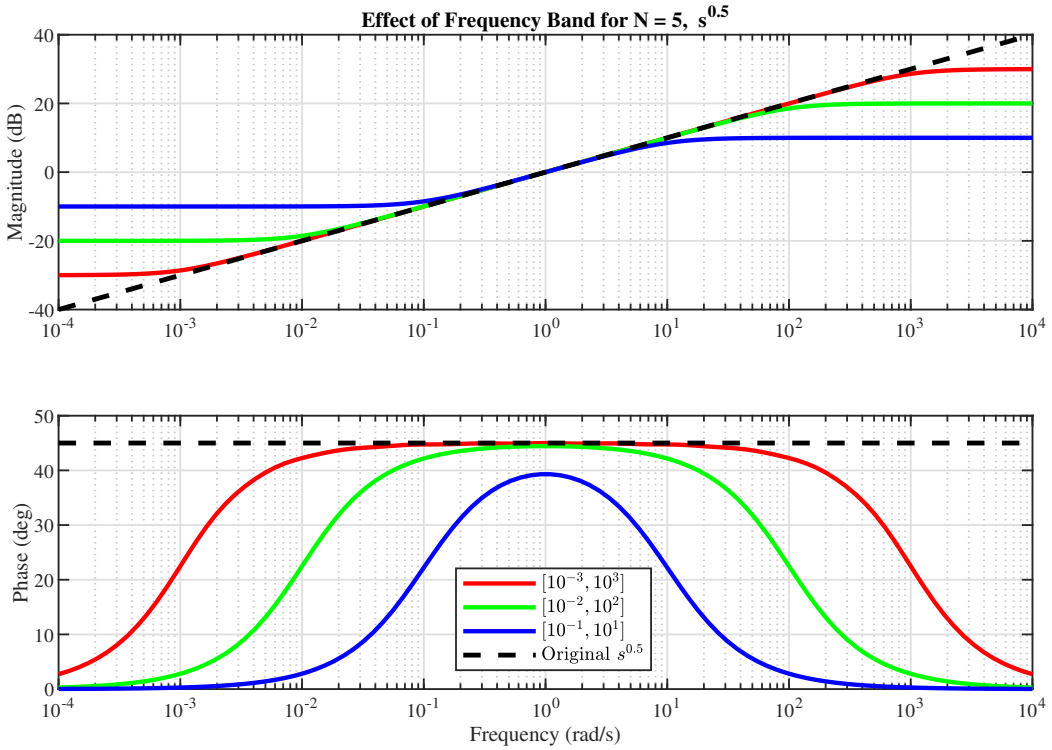


Figure 3. Bode magnitude and phase responses of the ORA models of $s^{0.5}$ for different frequency bands $[10^{-3}, 10^{3}]$, $[10^{-2}, 10^{2}]$, and $[10^{-1}, 10^{1}]$ rad/s with fixed approximation order $N = 5$.

Table 2. Frequency- and time-domain performance comparison of fifth-order recursive and refined Oustaloup approximation models of $s^{0.5}$ over different frequency bands.

ω_l	ω_h	RMSE_m (dB)		RMSE_p (deg)		Max_m (dB)		Max_p (deg)		IAE		ISE	
		ORA	ROA	ORA	ROA	ORA	ROA	ORA	ROA	ORA	ROA	ORA	ROA
10^{-3}	10^{3}	7.3549	4.3374	25.828	20.996	20	14.439	44.727	44.091	0.09153	0.38693	0.63805	5.9314
10^{-2}	10^{2}	13.46	9.6351	32.678	28.962	30	24.437	44.972	44.908	0.39295	0.24305	0.23298	0.024486
10^{-1}	10^{1}	20.696	16.213	38.415	35.26	40	34.437	44.997	44.991	3.0302	0.47211	1.284	0.50029

Overall, the results suggest that for ORA, the choice of frequency band is more influential than increasing the approximation order beyond a moderate value. A sufficiently wide design interval combined with a moderate order therefore provides the most reliable compromise between approximation quality and structural complexity.

3.2. Refined Oustaloup Approximation (ROA)

The refined Oustaloup approximation (ROA) extends the classical ORA by incorporating a correction filter intended to improve the approximation accuracy, particularly near the boundaries of the design frequency band [9,10,12,29]. This refinement is motivated by the observation that the standard recursive form may lose accuracy near the lower and upper cutoff frequencies, even when the interior band behavior remains satisfactory.

The ROA model is expressed as

$$G_{\mathrm{ROA}}(s) = K \prod_{k=-N}^{N} \frac{s+\omega'_k}{s+\omega_k} G_c(s), \tag{26}$$

where $G_c(s)$ denotes a correction filter of the form

$$G_c(s) = \frac{ds^2 + b\omega_H s}{d(1-\alpha)s^2 + b\omega_H s + d\alpha}. \tag{27}$$

In this study, the constants are chosen as $b = 10$ and $d = 9$, following the ROA implementation [9]. A comparison between the fifth-order standard and refined Oustaloup models is presented in Figure 4. The refined approximation exhibits improved magnitude and phase agreement over a wider portion of the frequency range, which is reflected in the broader effective accuracy bandwidth. In contrast, the standard ORA shows a narrower region of satisfactory approximation. The refined Oustaloup method consistently outperforms the recursive Oustaloup approximation, particularly in achieving closer alignment with the true system's magnitude and phase responses across a broader frequency range, as shown in Figure 4. However, for parameters $\omega_l = 0.001$ rad/s, $\omega_h = 1000$ rad/s, and $N = 3$ in the approximation of $s^{0.5}$, Equation (29) reveals that the refined Oustaloup's higher-order integer approximation introduces a transfer function of significantly higher order. While this improves accuracy, the resulting complexity may hinder analytical evaluation or real-time implementation in systems where computational efficiency is critical.

$$\begin{aligned} G_{\mathrm{ORA}}(s) = 31.623 & \frac{(s+0.001638)(s+0.01179)(s+0.08483)(s+0.6105)}{(s+0.004394)(s+0.03162)(s+0.2276)(s+1.638)} \\ & \times \frac{(s+4.394)(s+31.62)(s+227.6)}{(s+11.79)(s+84.83)(s+610.5)} \end{aligned} \tag{28}$$

$$\begin{aligned} G_{\mathrm{ROA}}(s) = 60s & \frac{(s+0.001638)(s+0.01179)(s+0.08483)(s+0.6105)}{(s+0.004394)(s+0.03162)(s+0.2276)(s+1.638)} \\ & \times \frac{(s+4.394)(s+31.62)(s+227.6)(s+1111)}{(s+11.79)(s+84.83)(s+610.5)(s+2222)(s+0.00045)} \end{aligned} \tag{29}$$

The numerical results in Table 1 confirm that ROA consistently improves frequency-domain accuracy, as indicated by lower RMSE and maximum error values in both magnitude and phase. At the same time, the standard ORA achieves lower IAE and ISE values, suggesting that improved frequency-domain matching does not automatically translate into superior time-domain performance. It is also evident that increasing the approximation order beyond $N = 5$ produces only a negligible improvement for both methods.

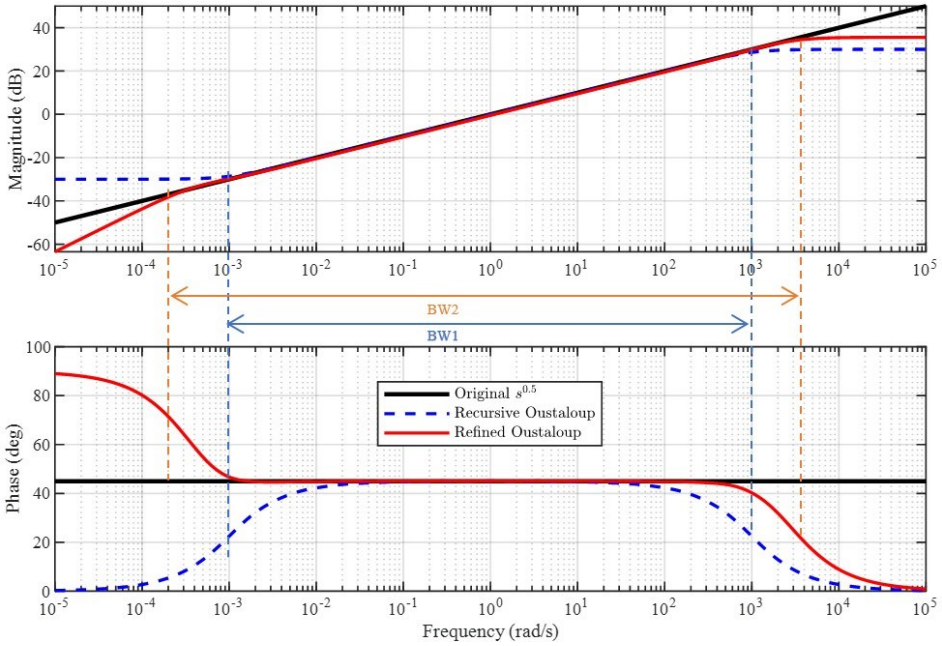


Figure 4. Comparison of Bode magnitude and phase responses for the fifth-order ORA and ROA models of $s^{0.5}$ over the frequency band $[10^{-3}, 10^{3}]$ rad/s.

The effect of the frequency band is summarized in Table 2. Across all tested bands, the ROA method yields lower RMSE and maximum errors than the standard version, confirming its superior frequency-domain accuracy. As the design band becomes narrower, the errors of both methods increase, but the refined approximation remains consistently more accurate. In the time domain, ROA provides lower IAE and ISE values for the medium and narrow bands, whereas ORA performs slightly better over the widest band $[10^{-3}, 10^{3}]$, again revealing a trade-off between frequency-domain precision and transient performance.

In summary, the main advantage of the Oustaloup family lies in its explicit frequency-band configurability, which makes it attractive for practical applications requiring approximation over a prescribed interval. However, this flexibility comes at the cost of increased model order, since an approximation of order N results in a transfer function of order $2N + 1$ in both the numerator and denominator. Consequently, although ROA generally improves frequency-domain behavior compared with ORA, both methods may become computationally demanding for higher-order implementations.

3.3. Continued Fraction Expansion (CFE)

The continued fraction expansion (CFE) method provides a rational approximation of the fractional-order operator s^{α} by expanding $(1 + x)^{\alpha}$ into a truncated continued fraction [12,17,25]:

$$(1+x)^{\alpha} \approx \cfrac{1}{1-\cfrac{\alpha x}{1+\cfrac{\frac{(1+\alpha)x}{1\cdot 2}}{1+\cfrac{\frac{(1-\alpha)x}{2\cdot 3}}{1+\cfrac{\frac{(2+\alpha)x}{3\cdot 4}}{1+\cfrac{\frac{(2-\alpha)x}{4\cdot 5}}{1+\cfrac{\frac{(3+\alpha)x}{5\cdot 6}}{1+\cfrac{\frac{(3-\alpha)x}{6\cdot 7}}{1+\ldots}}}}}}}} \tag{30}$$

The truncated terms of the first-order approximate CFE model of s^{α}, can be written as follows:

$$(1+x)^{\alpha} \approx \cfrac{1}{1-\cfrac{\alpha x}{1+\cfrac{(1+\alpha)x}{1\cdot 2}}} \approx \frac{2+(1+\alpha)x}{2+(1-\alpha)x} + \mathcal{O}(x^2) \tag{31}$$

By setting $x = s - 1$, where s represents the conventional integer-order Laplacian operator, the 1st-order approximation of s^α around a center frequency is given by a rational function:

$$s^\alpha \approx \frac{(1+\alpha)s + (1-\alpha)}{(1-\alpha)s + (1+\alpha)} \tag{32}$$

Through this construction, the fractional operator is represented by an integer-order transfer function, which makes the method attractive for practical realization when a relatively simple rational structure is desired. Table 3 summarizes the first- to fifth-order CFE models of s^α. As expected, increasing the approximation order produces a higher-order rational transfer function, which generally improves approximation accuracy while increasing implementation complexity.

Table 3. Continued fraction expansion (CFE) approximations of s^α for different orders [30].

Order	Terms	CFE Approximation of s^α
1	2	$\frac{(1+\alpha)s + (1-\alpha)}{(1-\alpha)s + (1+\alpha)}$
2	4	$\frac{(\alpha^2+3\alpha+2)s^2 + (-2\alpha^2+8)s + (\alpha^2-3\alpha+2)}{(\alpha^2-3\alpha+2)s^2 + (-2\alpha^2+8)s + (\alpha^2+3\alpha+2)}$
3	6	$\frac{(\alpha^3+6\alpha^2+11\alpha+6)s^3 + (-3\alpha^3-6\alpha^2+27\alpha+54)s^2 + (3\alpha^3-6\alpha^2+27\alpha+54)s + (-\alpha^3+6\alpha^2-11\alpha+6)}{(-\alpha^3+6\alpha^2-11\alpha+6)s^3 + (3\alpha^3-6\alpha^2+27\alpha+54)s^2 + (-3\alpha^3-6\alpha^2+27\alpha+54)s + (\alpha^3+6\alpha^2+11\alpha+6)}$
4	8	$\frac{\sum_{k=0}^{4} P_k s^{4-k}}{\sum_{k=0}^{4} Q_k s^{4-k}}$, where $\begin{cases} P_0 = Q_4 = \alpha^4 + 10\alpha^3 + 35\alpha^2 + 50\alpha + 24, \\ P_1 = Q_3 = -4\alpha^4 - 10\alpha^3 + 40\alpha^2 + 320\alpha + 384, \\ P_2 = Q_2 = 6\alpha^4 - 150\alpha^2 + 864, \\ P_3 = Q_1 = -4\alpha^4 + 20\alpha^3 + 40\alpha^2 - 320\alpha + 384, \\ P_4 = Q_0 = \alpha^4 - 10\alpha^3 + 35\alpha^2 - 50\alpha + 24 \end{cases}$
5	10	$\frac{\sum_{k=0}^{5} P_k s^{5-k}}{\sum_{k=0}^{5} Q_k s^{5-k}}$, where $\begin{cases} P_0 = Q_5 = -\alpha^5 - 15\alpha^4 - 85\alpha^3 - 225\alpha^2 - 274\alpha - 120, \\ P_1 = Q_4 = 5\alpha^5 + 45\alpha^4 + 5\alpha^3 - 1005\alpha^2 - 3250\alpha - 3000, \\ P_2 = Q_3 = -10\alpha^5 - 30\alpha^4 + 410\alpha^3 + 1230\alpha^2 - 4000\alpha - 12,000, \\ P_3 = Q_2 = 10\alpha^5 - 30\alpha^4 - 410\alpha^3 + 1230\alpha^2 + 4000\alpha - 12,000, \\ P_4 = Q_1 = -5\alpha^5 + 45\alpha^4 - 5\alpha^3 - 1005\alpha^2 + 3250\alpha - 3000, \\ P_5 = Q_0 = \alpha^5 - 15\alpha^4 + 85\alpha^3 - 225\alpha^2 + 274\alpha - 120 \end{cases}$

Figure 5 shows the Bode magnitude and phase responses of the first- to fourth-order CFE approximations of $s^{0.5}$. The results demonstrate that increasing the approximation order improves agreement with the ideal fractional operator. Lower-order models exhibit larger deviations and noticeable ripple behavior, particularly near the frequency-band boundaries, whereas higher-order models provide smoother responses and closer matching over a wider frequency interval.

To quantify the achievable approximation range, the effective bandwidth was determined directly from the Bode magnitude response using a ± 3 dB deviation criterion relative to the ideal fractional-order operator. Specifically, the lower and upper cutoff frequencies, ω_l and ω_h, were identified as the frequencies at which the magnitude error exceeded the ± 3 dB tolerance. The approximation bandwidth was then computed as

$$\Delta\omega = \omega_h - \omega_l. \tag{33}$$

This procedure provides a consistent and reproducible measure of the usable approximation region for each CFE order.

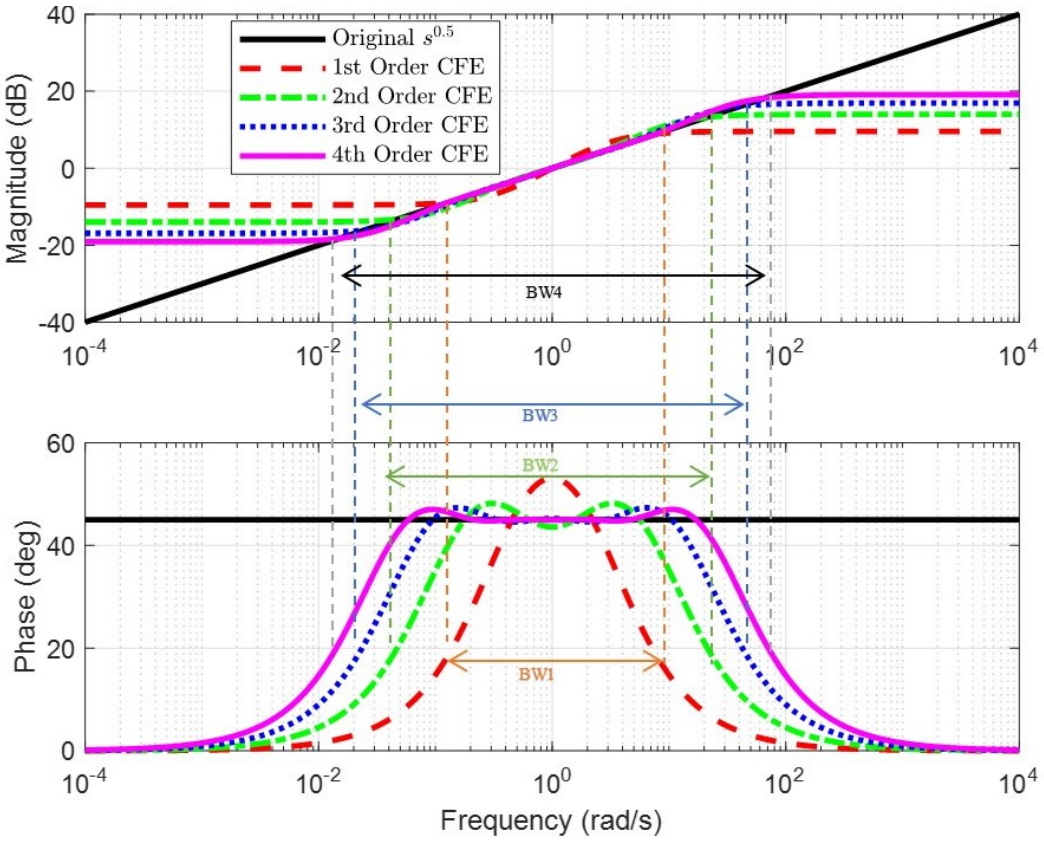


Figure 5. Bode magnitude and phase responses of first- to fourth-order CFE approximation models of $s^{0.5}$.

The quantitative results in Table 4 confirm the observed trend. Both magnitude and phase RMSE decrease as the approximation order increases, while the time-domain indices IAE and ISE also improve. In addition, the effective bandwidth expands significantly with model order. The fourth-order approximation achieves an upper frequency limit of approximately 53 rad/s and a bandwidth of 52.99 rad/s, exceeding the values reported in [17], where the maximum frequency and bandwidth were approximately 15 rad/s and 14.99 rad/s, respectively.

Table 4. Frequency- and time-domain performance of CFE approximations of $s^{0.5}$.

Order	Approx. T.F.	RMSE		Max		Time		Freq. and BW		
		Mag.	Phase	Mag.	Phase	IAE	ISE	ω_{min}	ω_{max}	BW
1	$s^{0.5} \approx \frac{3s+1}{s+3}$	15.383	37.978	30.458	44.98	2.993	1.367	0.13	7.8	7.67
2	$s^{0.5} \approx \frac{5s^2+10s+1}{s^2+10s+5}$	12.15	34.66	26.021	44.95	0.807	0.67	0.057	16	15.943
3	$s^{0.5} \approx \frac{7s^3+35s^2+21s+1}{s^3+21s^2+35s+7}$	10.17	32.406	23.098	44.908	0.236	0.46	0.02	34	33.78
4	$s^{0.5} \approx \frac{9s^4+84s^3+126s^2+36s+1}{s^4+36s^3+126s^2+84s+9}$	8.77	30.639	20.915	44.847	0.119	0.331	0.015	53	52.985

Unlike Oustaloup-based methods, the approximation range cannot be explicitly specified by the user and is instead determined implicitly by the order of the expansion (see

the last column of Table 4). Consequently, although higher-order CFE models improve the overall approximation and broaden the effective frequency range, the method offers limited flexibility when a predefined or application-specific frequency interval must be targeted.

Remark: A major drawback of the CFE approach is the absence of direct frequency-band tuning. As a result, the approximation error is distributed more uniformly across frequency, which may be acceptable for general-purpose approximation but less suitable for applications requiring focused accuracy over a user-defined range.

3.4. Matsuda's Approximation Method

Matsuda's approximation method is a frequency-domain approach that uses a continued fraction structure to approximate fractional-order operators by integer-order transfer functions. The method is especially attractive because it allows the approximation to be shaped through the selection of interpolation points over a prescribed frequency interval, which makes it suitable for applications where band-dependent accuracy is important [17,29].

A key feature of the Matsuda method is the use of logarithmically distributed frequency samples within a selected range $[\omega_l, \omega_h]$, defined as

$$\omega_k = \begin{cases} \omega_l \left(\frac{\omega_h}{\omega_l}\right)^{\frac{k-1}{n-1}}, & n > 1, \\ \omega_h, & n = 1, \end{cases} \tag{34}$$

where ω_l and ω_h denote the lower and upper frequency bounds, respectively, and n is the number of interpolation points. The magnitude response $|G(j\omega_k)|$ of the target fractional-order operator is then evaluated at these frequencies, after which a recursive interpolation process is used to compute the divided differences:

$$d_0(\omega_k) = |G(j\omega_k)|, \tag{35}$$

$$d_1(\omega_k) = \frac{d_0(\omega_k) - d_0(\omega_0)}{\omega_k - \omega_0}, \tag{36}$$

$$d_2(\omega_k) = \frac{d_1(\omega_k) - d_1(\omega_1)}{\omega_k - \omega_1}, \tag{37}$$

$$\vdots$$

$$d_n(\omega_k) = \frac{d_{n-1}(\omega_k) - d_{n-1}(\omega_{n-1})}{\omega_k - \omega_{n-1}}. \tag{38}$$

These divided differences are arranged in an upper triangular matrix D [29]:

$$D = \begin{bmatrix} d_0(\omega_0) & d_0(\omega_1) & \cdots & d_0(\omega_n) \\ 0 & d_1(\omega_1) & \cdots & d_1(\omega_n) \\ \vdots & \vdots & \ddots & \vdots \\ 0 & 0 & \cdots & d_n(\omega_n) \end{bmatrix}, \tag{39}$$

and the coefficients of the rational model are extracted from the diagonal terms as

$$\alpha_k = D_{kk}, \quad k = 0, 1, \ldots, n. \tag{40}$$

The approximation is then expressed in continued fraction form as

$$G_{\text{apx}}(s) = \alpha_0 + \cfrac{s-\omega_0}{\alpha_1 + \cfrac{s-\omega_1}{\alpha_2 + \cfrac{s-\omega_2}{\alpha_3 + \cdots}}}. \tag{41}$$

This formulation makes it possible to adapt the approximation to the selected frequency range, but it also means that the final result depends strongly on the chosen interpolation points and the adopted order. In this sense, Matsuda's method offers useful flexibility, although its performance is sensitive to the design setup.

Remark: Matsuda's method provides a good balance between flexibility and approximation capability, but its accuracy depends strongly on the choice of interpolation points, approximation order, and design frequency band.

Figures 6–9, together with Tables 5 illustrate the effect of approximation order and frequency band on the performance of the Matsuda method. When the approximation order is increased from $N = 3$ to $N = 8$, the frequency- and time-domain accuracy improves noticeably. As shown in Table 5, the magnitude RMSE decreases from 8.62 dB to 4.49 dB, and the IAE decreases from 0.34 to 0.005, indicating that higher-order Matsuda models provide significantly better approximation quality. However, the maximum phase error remains close to 44°, which shows that phase matching improves only moderately even when the order increases. Table 6 presents the Matsuda approximation of the fractional-order transfer function $s^{0.5}$.

Table 5. Performance metrics of Matsuda approximation for different orders of $s^{-0.5}$.

Order	RMSE		Max Error		Time Domain	
	Mag (dB)	Phase (deg)	Mag (dB)	Phase (deg)	IAE	ISE
3	8.62	30.61	20.681	44.84	0.34	0.01
5	6.43	27.27	16.98	44.62	0.01	0.00002
8	4.49	23.69	13.33	44.12	0.005	4.11×10^{-6}

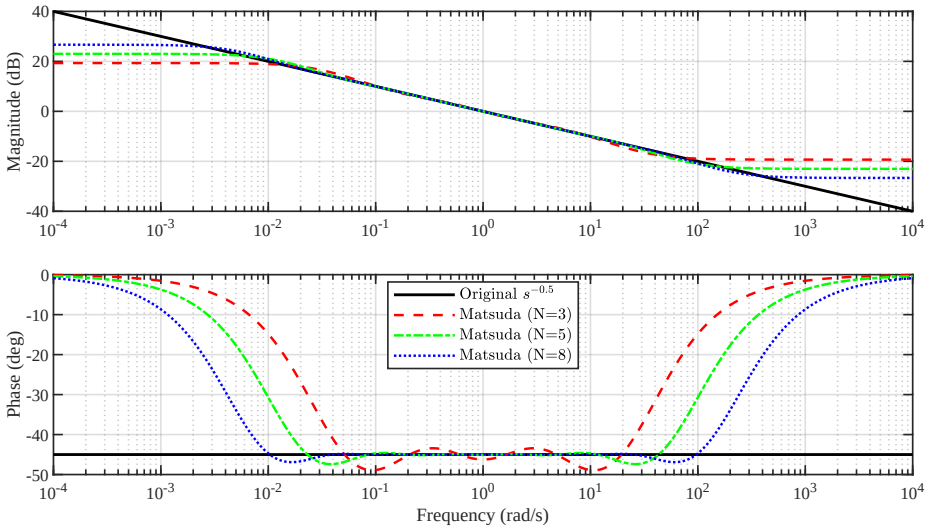


Figure 6. Bode magnitude and phase responses of the third-, fifth-, and eighth-order Matsuda approximation models of $s^{-0.5}$ over the frequency range $[10^{-3}, 10^{3}]$ rad/s.

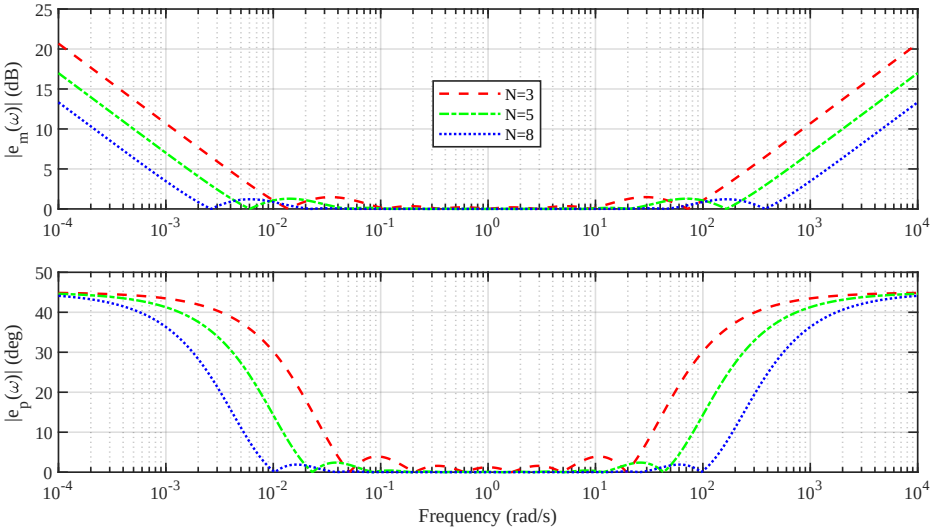


Figure 7. Magnitude and phase errors of the third-, fifth-, and eighth-order Matsuda approximation models of $s^{-0.5}$.

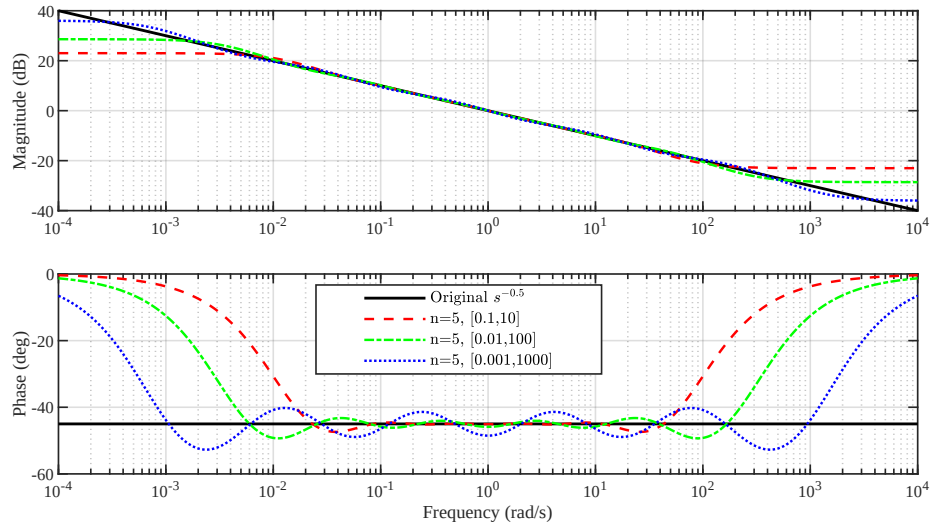


Figure 8. Bode magnitude and phase responses of the Matsuda approximation models of $s^{-0.5}$ for different frequency bands $[10^{-3}, 10^{3}]$, $[10^{-2}, 10^{2}]$, and $[10^{-1}, 10^{1}]$ rad/s with fixed approximation order $N = 5$.

Table 6. third- and fifth-order Matsuda approximation transfer functions of $s^{0.5}$.

Order (N)	Transfer Function $G(s)$
3	$s^{0.5} \approx \dfrac{9.2462s^3 + 61.2800s^2 + 33.4582s + 1}{s^3 + 33.4582s^2 + 61.2800s + 9.2462}$
5	$s^{0.5} \approx \dfrac{14.1541\,s^5 + 303.1615\,s^4 + 990.0340\,s^3 + 671.7605\,s^2 + 86.7055\,s + 1}{s^5 + 86.7055\,s^4 + 671.7605\,s^3 + 990.0340\,s^2 + 303.1615\,s + 14.1541}$

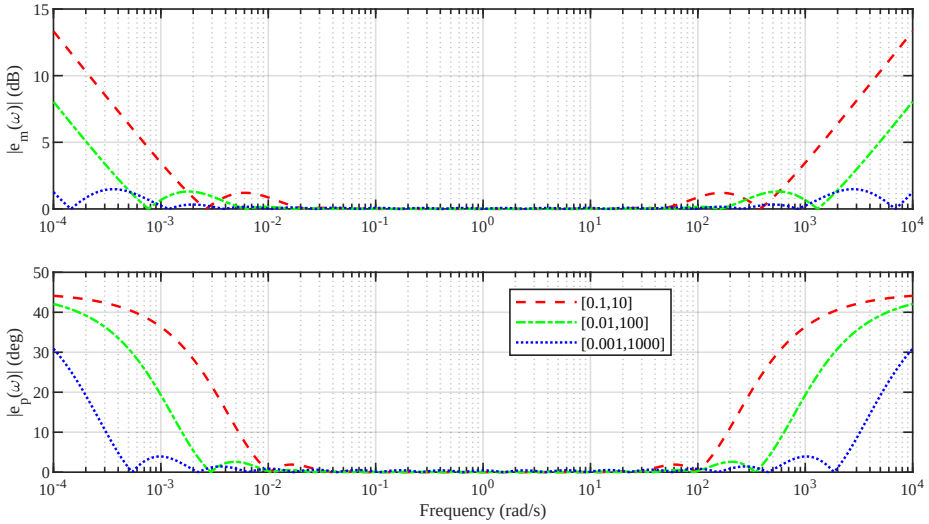


Figure 9. Magnitude and phase errors of the Matsuda approximation models of $s^{-0.5}$ for different frequency bands $[10^{-3}, 10^{3}]$, $[10^{-2}, 10^{2}]$, and $[10^{-1}, 10^{1}]$ rad/s with fixed approximation order $N = 5$.

The effect of the design frequency band is presented in Table 7. With fixed order $N = 5$, expanding the frequency range from $[10^{-1}, 10^{1}]$ to $[10^{-3}, 10^{3}]$ rad/s substantially reduces the frequency-domain errors. In particular, the magnitude RMSE decreases from 6.43 dB to 1.10 dB. However, this improvement is accompanied by deterioration in the time domain, as the IAE increases from 0.01 to 0.97. Therefore, a wider band improves global frequency-domain fitting but leads to a poorer transient response.

Table 7. Performance metrics of Matsuda approximation for different frequency bands of $s^{-0.5}$ with fixed order $N = 5$.

Frequency (rad/s)		RMSE		Max Error		Time Domain	
ω_l	ω_h	Mag (dB)	Phase (deg)	Mag (dB)	Phase (deg)	IAE	ISE
0.1	10	6.43	27.27	16.98	44.62	0.01	2.32×10^{-5}
0.01	100	3.58	21.93	11.39	43.71	0.15	0.001
0.001	1000	1.10	13.37	4.03	38.46	0.97	0.06

The results in Table 7 present a clear trade-off between frequency-domain accuracy and time-domain performance as the approximation bandwidth increases. For a fixed approximation order $N = 5$, widening the frequency interval improves the global fitting accuracy of the fractional operator, as evidenced by the reduction in RMSE and maximum frequency-domain errors. This improvement occurs because the approximation is optimized over a broader spectral range, enabling better matching of the operator dynamics across low-, mid-, and high-frequency regions.

However, the improvement in frequency-domain accuracy is accompanied by degradation in time-domain performance, reflected by increased IAE and ISE values. This behavior arises because the same finite-order approximation must distribute a limited number of poles and zeros across a larger frequency interval. Consequently, fewer degrees of freedom remain available to accurately capture localized transient dynamics.

This phenomenon is closely related to the time–frequency trade-off commonly observed in signal analysis and approximation theory [31]. Similar to the uncertainty principle, improving spectral accuracy over a wide frequency band reduces temporal localization capability. Therefore, a wider frequency band enhances global frequency matching but may

deteriorate transient response quality. Conversely, a narrower band concentrates approximation fidelity around dominant frequencies, often resulting in improved time-domain behavior at the expense of reduced broadband accuracy.

Taken together, these results show that Matsuda's approximation is highly dependent on both approximation order and frequency-band selection. Increasing the order generally improves accuracy, whereas widening the frequency interval enhances global frequency matching at the expense of time-domain performance. The method is therefore flexible and practically useful, but it requires careful tuning when applied to control-oriented problems.

3.5. El-Khazali Approximations

The El-Khazali method provides practical rational approximations of the fractional-order operator s^α using both first- and second-order models and is particularly attractive because it offers relatively simple realizations while still preserving the main dynamic characteristics of the ideal fractional operator [32–35]. In contrast to higher-order approximation schemes, this method is especially useful when a compact structure is preferred for implementation.

The first-order approximation replaces the fractional operator s^α, with $0 < \alpha < 1$, by the rational transfer function

$$s^\alpha \approx \frac{N(s,\alpha)}{D(s,\alpha)} = \frac{\frac{s\tau}{\omega_{cn}} + 1}{\frac{s}{\omega_{cn}} + \tau}, \tag{42}$$

where ω_{cn} denotes the corner frequency and τ is defined as

$$\tau = \tan\left(\frac{\alpha\pi}{2}\right) + \sec\left(\frac{\alpha\pi}{2}\right). \tag{43}$$

This approximation is computationally efficient and straightforward to implement, which makes it attractive in applications where low-order realization is more important than wideband accuracy.

To improve approximation accuracy, El-Khazali further proposed a second-order rational model based on a cascade of biquadratic transfer functions [35]. In this formulation, the fractional operator is represented as

$$\left(\frac{s}{\omega_g}\right)^\alpha = \prod_{i=1}^{n} F_i\left(\frac{s}{\omega_i}\right) = \prod_{i=1}^{n} \frac{N_i\left(\frac{s}{\omega_i}\right)}{D_i\left(\frac{s}{\omega_i}\right)}, \tag{44}$$

where ω_i is the center frequency of the i-th biquadratic stage, and

$$\omega_g = \sqrt[n]{\prod_{i=1}^{n} \omega_i} \tag{45}$$

is the geometric mean of all center frequencies.

For $i \geq 2$, the subsequent center frequencies are recursively determined by

$$\omega_i = \omega_x^{2^{(i-1)}} \omega_1, \qquad i = 2, 3, \ldots, n, \tag{46}$$

where ω_x is the real root of the characteristic polynomial

$$a_0 a_2 \eta^4 \lambda^4 + a_1(a_2 - a_0)\lambda^3 + (a_1^2 - a_2^2 - a_0^2)\eta\lambda^2 + a_1(a_2 - a_0)\lambda + a_0 a_2 \eta = 0, \tag{47}$$

with

$$\eta = \tan\left(\frac{\alpha\pi}{4}\right). \tag{48}$$

Each biquadratic transfer function F_i is then given by

$$F_i\left(\frac{s}{\omega_i}\right) \approx \frac{a_0\left(\frac{s}{\omega_i}\right)^2 + a_1\left(\frac{s}{\omega_i}\right) + a_2}{a_2\left(\frac{s}{\omega_i}\right)^2 + a_1\left(\frac{s}{\omega_i}\right) + a_0}, \tag{49}$$

where the coefficients a_0, a_1, and a_2 are defined as

$$a_0 = \alpha^\alpha + 3\alpha + 1, \tag{50}$$

$$a_2 = \alpha^\alpha - 3\alpha + 1, \tag{51}$$

$$a_1 = (a_2 - a_0)\tan\left(\frac{(2+\alpha)\pi}{4}\right) = -6\alpha\tan\left(\frac{(2+\alpha)\pi}{4}\right). \tag{52}$$

For the special case $\omega_i = 1$, the second-order approximation reduces to

$$s^\alpha \approx \frac{a_0 s^2 + a_1 s + a_2}{a_2 s^2 + a_1 s + a_0}. \tag{53}$$

Moreover, when $\alpha \to 1$, the approximation simplifies to

$$F_i\left(\frac{s}{\omega_i}\right) \approx \frac{a_0\left(\frac{s}{\omega_i}\right)^2 + a_0\left(\frac{s}{\omega_i}\right)}{a_0\left(\frac{s}{\omega_i}\right)^2 + a_0}. \tag{54}$$

Overall, the El-Khazali approximations provide a useful low-order alternative for fractional-order realization. The first-order form is attractive for its simplicity, whereas the second-order formulation offers improved dynamic fidelity while still preserving a relatively compact structure.

3.6. Charef Approximation Method

The Charef approximation method provides a practical approach for approximating fractional-order operators by means of rational transfer functions defined over a prescribed frequency range [14,36]. The method is primarily intended for the approximation of the fractional-order integrator

$$H(s) = \frac{1}{s^\alpha}, \qquad 0 < \alpha < 1, \tag{55}$$

and is based on a logarithmic distribution of real poles and zeros over the selected frequency interval (ω_l, ω_h). A distinctive feature of this method is that the approximation accuracy is controlled explicitly by a user-defined magnitude error bound Δ expressed in decibels.

The resulting rational approximation is written as

$$H_{\mathrm{ch}}(s) = \frac{1}{s^\alpha} \approx \frac{\prod_{k=0}^{N-1}\left(1 + \frac{s}{z_k}\right)}{\prod_{k=0}^{N}\left(1 + \frac{s}{p_k}\right)}, \tag{56}$$

where z_k and p_k denote the zeros and poles, respectively.

The parameters governing the pole-zero spacing are defined as

$$a = 10^{\frac{\Delta}{10(1-\alpha)}}, \qquad b = 10^{\frac{\Delta}{10\alpha}}, \qquad ab = 10^{\frac{\Delta}{10\alpha(1-\alpha)}}, \tag{57}$$

which directly determine the logarithmic separation between successive poles and zeros. The poles and zeros are then given by

$$\begin{aligned} p_0 &= \omega_l \cdot 10^{\frac{\Delta}{20\alpha}}, \\ p_k &= (ab)^k p_0, \\ z_k &= a(ab)^k p_0, \qquad k = 0, 1, \ldots, N-1, \end{aligned} \tag{58}$$

thus ensuring a structured logarithmic distribution across the frequency band.

The required approximation order N is determined by

$$N = \left\lfloor \frac{\log\left(\frac{\omega_h}{p_0}\right)}{\log(ab)} \right\rfloor + 1, \tag{59}$$

where $\lfloor \cdot \rfloor$ denotes the integer part. This relation links the desired frequency range, the allowed error, and the final order of the approximation.

Charef Approximation Version 2 [37] extends the same concept to the approximation of a first-order fractional system, namely,

$$H(s) = \frac{1}{\left(1 + \frac{s}{\omega_l}\right)^{\alpha}} \approx \frac{\prod_{k=0}^{N-1}\left(1 + \frac{s}{z_k}\right)}{\prod_{k=0}^{N}\left(1 + \frac{s}{p_k}\right)}, \qquad 0 < \alpha < 1. \tag{60}$$

The Charef method is therefore attractive when an explicit bound on magnitude error is required over a prescribed band, although its practical effectiveness depends strongly on the selected frequency interval and target accuracy. To generalize the Charef approximation, a fractional-order system can be decomposed into two components [38,39]:

$$G(s) = G_{\alpha}(s)\, G_{\beta}(s) \tag{61}$$

where

$$G_{\alpha}(s) = \frac{1}{(T_{\alpha} s + 1)^{\alpha}}, \quad G_{\beta}(s) = (T_{\beta} s + 1)^{\beta} = \frac{1}{\frac{1}{(T_{\beta} s + 1)^{\beta}}}. \tag{62}$$

Each component is approximated independently using the Charef formulation:

$$G_{\mathrm{ch},\alpha}(s) = \frac{\prod_{k=0}^{N_{\alpha}-1}\left(1 + \frac{s}{z_k^{(\alpha)}}\right)}{\prod_{k=0}^{N_{\alpha}-1}\left(1 + \frac{s}{p_k^{(\alpha)}}\right)} = \frac{L_{\alpha}(s)}{D_{\alpha}(s)}, \tag{63}$$

$$G_{\mathrm{ch},\beta}(s) = \frac{\prod_{k=0}^{N_{\beta}-1}\left(1 + \frac{s}{z_k^{(\beta)}}\right)}{\prod_{k=0}^{N_{\beta}-1}\left(1 + \frac{s}{p_k^{(\beta)}}\right)} = \frac{D_{\beta}(s)}{L_{\beta}(s)}. \tag{64}$$

The overall approximation is then obtained as

$$G_{\mathrm{ch}}(s) = G_{\mathrm{ch},\alpha}(s)\, G_{\mathrm{ch},\beta}(s) = \frac{L_{\alpha}(s)\, D_{\beta}(s)}{D_{\alpha}(s)\, L_{\beta}(s)}, \tag{65}$$

with the total approximation order given by $N = N_\alpha + N_\beta - 1$. The individual orders are determined as

$$N_\alpha = \left\lfloor \frac{10\alpha(1-\alpha)\,\log(\omega_{\max} T_\alpha)}{\Delta} \right\rfloor + 1,$$
$$N_\beta = \left\lfloor \frac{10\beta(1-\beta)\,\log(\omega_{\max} T_\beta)}{\Delta} \right\rfloor + 1. \tag{66}$$

This formulation ensures a bounded approximation error governed by the tolerance Δ, while typically achieving lower actual deviations in practice. However, the presence of pole–zero cancellations may introduce localized errors, particularly near the boundaries of the frequency range.

To illustrate the application of this method, consider the fractional-order transfer function

$$G(s) = \frac{(8s+1)^{0.5}}{(49s+1)^{0.6}}, \tag{67}$$

which consists of a fractional numerator and denominator. Using the Charef approach, the system is decomposed into two components corresponding to the numerator and denominator dynamics. The approximation orders N_α and N_β are computed independently based on the specified error tolerance, and the total order is given by $N = N_\alpha + N_\beta - 1$.

Figure 10 presents the Bode magnitude responses of the resulting approximations for different error tolerances $\Delta = [1, 2, 3]$ dB. It can be observed that lower tolerance values yield higher-order models that closely match the ideal fractional-order response across the frequency range. In contrast, increasing Δ reduces the approximation order and simplifies the model but introduces noticeable deviations, particularly at higher frequencies. This behavior clearly demonstrates the trade-off between approximation accuracy and computational complexity inherent in the Charef method.

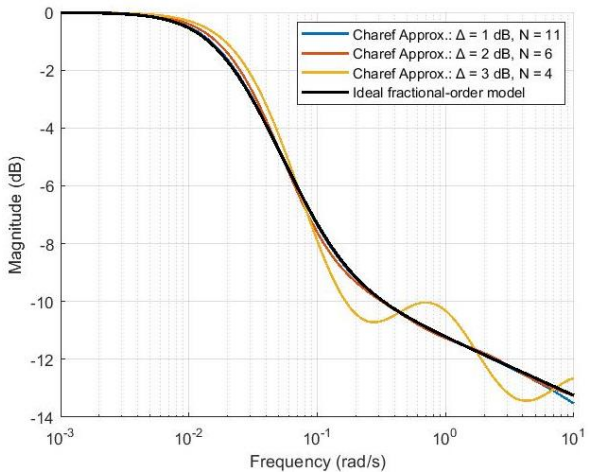


Figure 10. Magnitude response of the Charef approximation for different error tolerances $\Delta = 1, 2, 3$ dB for transfer function stated in Equation (67).

Table 8 summarizes the magnitude error metrics of the Charef approximation for the composite fractional-order system. The results indicate that decreasing the error tolerance Δ improves the approximation accuracy, as reflected by the reduction in RMSE_m and maximum magnitude error.

For $\Delta = 1$ dB, the approximation achieves the highest accuracy with $\text{RMSE}_m = 0.0603$ dB but requires a higher total order ($N = 11$), resulting from $N_\alpha = 7$ and $N_\beta = 5$. As Δ increases, the approximation order decreases significantly, leading to reduced computational complexity. However, this simplification comes at the expense of accuracy, particularly evident for $\Delta = 3$ dB, where both RMSE and maximum error increase substantially.

Table 8. Magnitude error analysis of the Charef composite approximation for different error tolerances.

Δ (dB)	N_α	N_β	N	RMSE$_m$ (dB)	Max$_m$ (dB)
1	7	5	11	0.0603	0.2797
2	4	3	6	0.1388	0.3005
3	3	2	4	0.6104	1.2754

These results confirm that the Charef method provides a flexible trade-off between accuracy and model complexity, which becomes more pronounced in composite fractional-order systems involving both numerator and denominator dynamics.

3.7. Carlson's Approximation

Carlson's approximation [6] provides an iterative framework for approximating fractional-order operators by computing the α-th root of a given transfer function $G(s)$. The method is based on a modified Newton–Raphson scheme and is particularly suitable for constructing rational approximations of operators that are inherently non-rational.

For the α-th root problem, the objective is to determine a function $H(s)$ such that

$$H(s) = (G(s))^{\alpha}. \tag{68}$$

By defining the nonlinear function $f(H) = H^{\alpha} - G(s)$, the classical Newton–Raphson update becomes

$$H_k = H_{k-1} - \frac{H_{k-1}^{\alpha} - G(s)}{\alpha H_{k-1}^{\alpha-1}}. \tag{69}$$

To improve numerical stability and convergence behavior, this update can be reformulated in multiplicative form. After algebraic manipulation, the iteration is written as

$$H_k(s) = H_{k-1}(s) \cdot \frac{(1-\alpha)H_{k-1}(s)^{1/\alpha} + (1+\alpha)G(s)}{(1+\alpha)H_{k-1}(s)^{1/\alpha} + (1-\alpha)G(s)}. \tag{70}$$

Introducing the substitution $Q(s) = H_{k-1}(s)^{1/\alpha}$, the same update can be expressed as

$$\begin{aligned} H_k(s) &= H_{k-1}(s) \cdot \frac{(1-\alpha)Q(s) + (1+\alpha)G(s)}{(1+\alpha)Q(s) + (1-\alpha)G(s)} \\ &= \frac{Q(s)^{\alpha}[(1-\alpha)Q(s) + (1+\alpha)G(s)]}{(1+\alpha)Q(s) + (1-\alpha)G(s)}. \end{aligned}$$

Since $Q(s)^{\alpha} = H_{k-1}(s)$, this representation remains fully consistent with the original Newton–Raphson formulation while offering a more numerically stable iterative realization.

Carlson Iteration Algorithm:

1. Initialize $H_0(s) = 1$.
2. For $k = 1, 2, \ldots, N$:
   (a) Compute $Q(s) = H_{k-1}(s)^{1/\alpha}$.
   (b) Update $H_k(s)$ using (70).
3. Return $H_N(s)$ as the final approximation.

Carlson's method is mathematically elegant and can provide accurate results through successive iterations; however, its iterative nature may increase computational effort compared with direct closed-form approximation methods, especially when higher precision is required.

3.8. Curve-Fitting Approximation

The curve-fitting approach, reported in [15], constructs an integer-order approximation of a fractional operator by directly fitting its frequency response data. Unlike analytical approximation methods, this technique is data-driven and relies on matching the frequency-domain behavior of s^α over a specified range.

The procedure begins by generating the frequency response of the fractional operator through the substitution $s = j\omega$ over a logarithmically spaced frequency grid $\omega \in [\omega_L, \omega_H]$:

$$s^\alpha = (j\omega)^\alpha, \quad \omega = \omega_L, \omega_{L+1}, \ldots, \omega_H. \tag{71}$$

Using this frequency response data (FRD), an integer-order transfer function is identified via the iterative Sanathanan–Koerner (SK) algorithm [16]. The approximating model is expressed as

$$G(s) = \frac{P(s)}{Q(s)} = \frac{\mathbf{P}^T \boldsymbol{\phi}(s)}{1 + \mathbf{Q}^T \boldsymbol{\psi}(s)}, \tag{72}$$

where the numerator and denominator polynomials are defined as $P(s) = \sum_{n=0}^{N} p_n s^n$ and $Q(s) = 1 + \sum_{n=1}^{N} q_n s^n$. The coefficient vectors $\mathbf{P}$ and $\mathbf{Q}$ are constructed using the basis vectors

$$\boldsymbol{\phi}(s) = [1, s, \ldots, s^N]^T, \quad \boldsymbol{\psi}(s) = [s, s^2, \ldots, s^N]^T.$$

The unknown parameters are estimated by minimizing the weighted least-squares cost function

$$\min_{\mathbf{P},\mathbf{Q}} \sum_{k=1}^{H} \left| \frac{\boldsymbol{\phi}^T(j\omega_k)\mathbf{P}^{(\ell)} - (j\omega_k)^\alpha \boldsymbol{\psi}^T(j\omega_k)\mathbf{Q}^{(\ell)}}{Q^{(\ell-1)}(j\omega_k)} \right|^2, \tag{73}$$

where $Q^{(\ell-1)}(s) = 1 + \boldsymbol{\psi}^T(s)\mathbf{Q}^{(\ell-1)}$. The iterative process continues until convergence is achieved, typically defined by

$$\|\mathbf{Q}^{(\ell)} - \mathbf{Q}^{(\ell-1)}\|_2 < \epsilon,$$

with ϵ denoting a prescribed tolerance.

Implementation Procedure:

1. Frequency Sampling: Generate FRD data of s^α over the desired frequency range.
2. Iterative Identification: Apply the SK algorithm to estimate $\mathbf{P}$ and $\mathbf{Q}$ through weighted least-squares minimization.
3. Convergence Check: Terminate the iteration when $\|\mathbf{Q}^{(\ell)} - \mathbf{Q}^{(\ell-1)}\|_2 < \epsilon$.
4. Model Construction: Form the rational transfer function $G(s) = P^{(K)}(s)/Q^{(K)}(s)$.
5. State-Space Realization: Convert the model into state-space form:

$$G(s) = \mathbf{C}(s\mathbf{I} - \mathbf{A})^{-1}\mathbf{B} + D.$$

6. Model Reduction: Apply pole–zero cancellation to obtain a minimal realization:

$$G(s) = \texttt{minreal}\left(\frac{\sum_{n=0}^{N} p_n^{(K)} s^n}{1 + \sum_{n=1}^{N} q_n^{(K)} s^n} \right).$$

where `minreal` is a MATLAB function that computes a minimal realization of a transfer function.

Remark: This approach offers high flexibility and can achieve very accurate approximations when sufficient data and model order are used; however, its performance depends strongly on the quality of the sampled data and the chosen model structure, and it may suffer from overfitting or numerical sensitivity.

3.9. Modified Stability Boundary Locus (M-SBL) Approximation

This subsection presents an enhanced version of the stability boundary locus (SBL) method originally introduced in [40] and further developed in [17,18]. The SBL-based approach approximates the fractional-order operator s^α by matching its stability boundary locus with that of an equivalent integer-order model.

In the original formulation, the approximation parameters were obtained through two separate linear systems derived from the real and imaginary parts of the characteristic equation, which increased computational complexity and limited implementation efficiency. The modified approach addresses this limitation by solving both components simultaneously within a unified framework.

Consider a fractional-order system described by

$$s^\alpha + as^\beta + b = 0, \quad \alpha > \beta \in \mathbb{R}^+. \tag{74}$$

By substituting $s = j\omega$, the stability boundary locus is expressed as

$$\Re: \quad \omega^\alpha \cos\left(\frac{\alpha\pi}{2}\right) + a\omega^\beta \cos\left(\frac{\beta\pi}{2}\right) + b = 0, \tag{75}$$

$$\Im: \quad \omega^\alpha \sin\left(\frac{\alpha\pi}{2}\right) + a\omega^\beta \sin\left(\frac{\beta\pi}{2}\right) = 0. \tag{76}$$

The modified stability boundary locus (M-SBL) method solves these equations jointly, which improves numerical efficiency and enhances robustness. In addition, the use of a logarithmically spaced frequency grid contributes to better approximation accuracy over a wider range.

The objective is to approximate s^α by an integer-order rational transfer function of the form

$$G_{\text{apx}}(s) = \frac{\sum_{k=0}^{n} c_k s^k}{\sum_{k=0}^{n} d_k s^k}, \tag{77}$$

such that

$$G_{\text{apx}}(j\omega) \approx (j\omega)^\alpha = \omega^\alpha \left[\cos\left(\frac{\alpha\pi}{2}\right) + j\sin\left(\frac{\alpha\pi}{2}\right)\right]. \tag{78}$$

For an n-th order model evaluated at frequency ω_k, this leads to

$$\sum_{r=0}^{n} c_r (j\omega_k)^r = (j\omega_k)^\alpha \sum_{r=0}^{n} d_r (j\omega_k)^r. \tag{79}$$

By imposing denominator symmetry $d_r = c_{n-r}$, the problem is reduced to a linear system

$$\mathbf{AC} = \mathbf{B}, \tag{80}$$

where

$$\mathbf{C} = [c_0, c_1, \ldots, c_n]^T.$$

The matrix elements for each frequency ω_k are defined as

$$A_{rk} = (j\omega_k)^r - (j\omega_k)^{n-r+2} \frac{\cos\left(\frac{\alpha\pi}{2}\right)}{\omega_k^\alpha} - (j\omega_k)^{n-r+1} \frac{\sin\left(\frac{\alpha\pi}{2}\right)}{\omega_k^{\alpha-1}}, \tag{81}$$

$$B_k = -(j\omega_k)^{n+1} + (j\omega_k) \frac{\cos\left(\frac{\alpha\pi}{2}\right)}{\omega_k^\alpha} + \frac{\sin\left(\frac{\alpha\pi}{2}\right)}{\omega_k^{\alpha-1}}. \tag{82}$$

The coefficient vector is then obtained as

$$\mathbf{C} = (\mathbf{A}^{-1})^T \mathbf{B}^T, \tag{83}$$

and the final approximation becomes

$$G_{\text{apx}}(s) = \frac{\sum_{k=0}^{n} c_k s^k}{\sum_{k=0}^{n} c_{n-k} s^k}. \tag{84}$$

To quantify the numerical expense of the M-SBL method, the condition number of the coefficient matrix A and the execution time were evaluated for different approximation orders. The condition number is defined as

$$\kappa(A) = \|A\| \, \|A^{-1}\|, \tag{85}$$

where a larger value of $\kappa(A)$ indicates stronger numerical ill-conditioning and higher sensitivity to perturbations in the coefficient matrix.

Table 9 shows that increasing the M-SBL order improves approximation accuracy, as RMSE_m decreases from 6.0757 dB at $N = 2$ to 0.2882 dB at $N = 12$. Similarly, RMSE_p decreases from 26.024° to 6.4084°. However, this improvement is accompanied by a substantial increase in the condition number, from 1.0488×10^{12} at $N = 2$ to 3.0490×10^{51} at $N = 12$. This indicates that higher-order M-SBL approximations become increasingly ill-conditioned, even though the measured execution time remains relatively small, as given in Figure 11.

Table 9. Numerical conditioning and computational cost of the M-SBL approximation for $G(s) = s^{0.5}$.

Order N	$\kappa(A)$	Time (s)	RMSE_m	RMSE_p
2	1.0488×10^{12}	0.0049	6.0757	26.024
3	2.9150×10^{15}	0.0005	3.8522	19.094
4	1.9579×10^{19}	0.0021	2.2259	14.683
5	2.5546×10^{21}	0.0016	1.4770	12.807
6	1.4686×10^{28}	0.0015	1.0494	11.660
7	1.2387×10^{30}	0.0017	0.7724	10.698
8	9.8008×10^{35}	0.0018	0.5791	9.7819
9	6.3941×10^{36}	0.0017	0.4431	8.8890
10	1.4592×10^{42}	0.0015	0.3540	8.0238
11	3.5195×10^{43}	0.0012	0.3054	7.1947
12	3.0490×10^{51}	0.0017	0.2882	6.4084

These results confirm that M-SBL is not computationally expensive only in terms of execution time; its main numerical limitation is the conditioning of the linear system used to compute the approximation coefficients. Therefore, the approximation order should be selected carefully to balance accuracy improvement against numerical sensitivity. In this study, moderate orders provide a more reliable compromise between accuracy, computational cost, and numerical conditioning.

Figure 12 shows the Bode plots for the magnitude and phase, comparing the true system with the M-SBL and curve-fitting approximations for $N = 4, 5, 6$. The plots illustrate the performance of both approximation methods across different orders and their comparison with the true fractional-order system. The respective transfer functions for each approximation method are provided in Table 10.

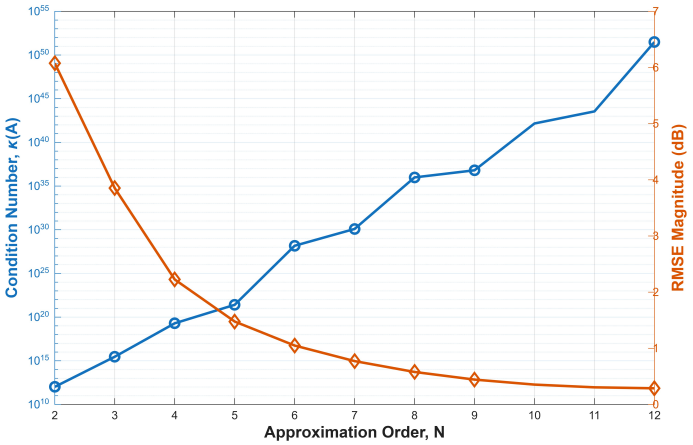


Figure 11. M-SBL Accuracy and Numerical Conditioning Trade-off for $s^{0.5}$.

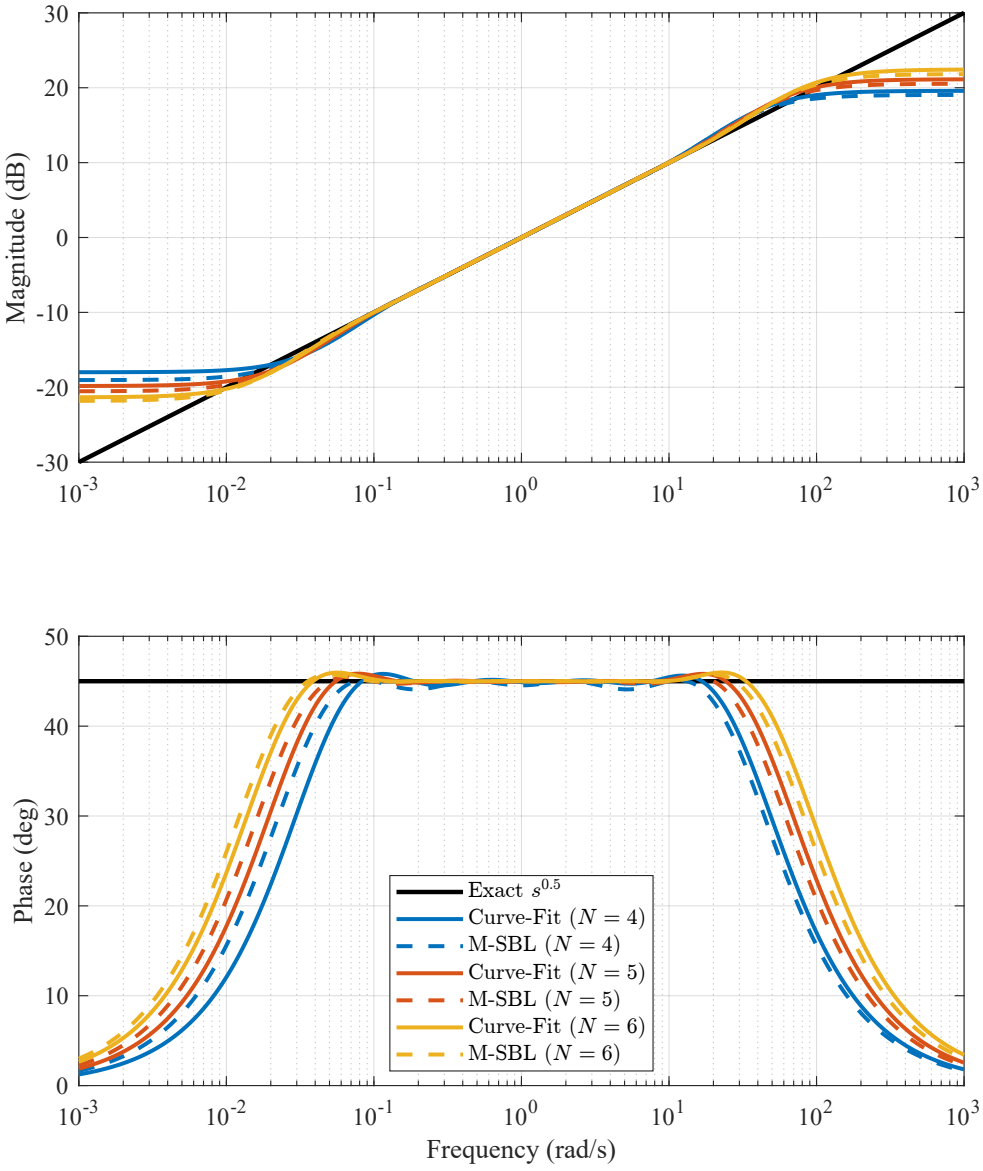


Figure 12. Bode plot comparison between the true fractional-order system $s^{0.5}$ and its M-SBL and curve-fitting approximations for orders $N = 4$ to 6. The magnitude and phase responses highlight the accuracy and frequency-domain behavior of each approximation method relative to the true model. As the approximation order increases, the M-SBL approximations better align with the true system, especially within the frequency range $[\omega_l = 0.1,\ \omega_h = 10]$.

Table 10. Transfer Functions of M-SBL and Curve-Fitting Approximations for $s^{0.5}$ at Different Orders.

N	M-SBL Transfer Function	Curve-Fitting Transfer Function
4	$s^{0.5} \approx \frac{8.9586\,s^4+99.124\,s^3+155.24\,s^2+39.628\,s+1}{s^4+39.628\,s^3+155.24\,s^2+99.124\,s+8.9586}$	$s^{0.5} \approx \frac{9.5396\,s^4+118.75\,s^3+230.74\,s^2+77.934\,s+2.6163}{s^4+43.907\,s^3+204.96\,s^2+168.96\,s+20.761}$
5	$s^{0.5} \approx \frac{10.644\,s^5+177.85\,s^4+534.21\,s^3+372.47\,s^2+56.144\,s+1}{s^5+56.144\,s^4+372.47\,s^3+534.21\,s^2+177.85\,s+10.644}$	$s^{0.5} \approx \frac{11.396\,s^5+214.79\,s^4+761.60\,s^3+646.41\,s^2+120.22\,s+2.5880}{s^5+63.347\,s^4+486.16\,s^3+838.12\,s^2+343.00\,s+25.384}$
6	$s^{0.5} \approx \frac{12.354\,s^6+288.47\,s^5+1390.4\,s^4+1884.0\,s^3+749.81\,s^2+75.806\,s+1}{s^6+75.806\,s^5+749.81\,s^4+1884.0\,s^3+1390.4\,s^2+288.47\,s+12.354}$	$s^{0.5} \approx \frac{13.251\,s^6+350.04\,s^5+1948.8\,s^4+3092.9\,s^3+1447.2\,s^2+171.06\,s+2.5715}{s^6+86.212\,s^5+975.41\,s^4+2854.7\,s^3+2475.4\,s^2+602.99\,s+30.019}$

To investigate the influence of sampling density on approximation quality, a sensitivity analysis was conducted by varying the number of logarithmically distributed frequency points used in Matsuda, curve-fitting, and M-SBL methods. The resulting accuracy and computational cost are summarized in Table 11.

Table 11. Effect of selected frequency points on approximation performance for Matsuda, curve-fitting, and M-SBL methods.

Order	Matsuda			Curve Fit			M-SBL		
	Points	RMSE_m	Time (s)	Points	RMSE_m	Time (s)	Points	RMSE_m	Time (s)
1	3	2.6947	0.0077	3	3.3368	0.0048	1	4.8390	0.0015
2	5	0.7246	0.0098	5	1.3955	0.0033	2	1.1554	0.0014
3	7	0.1956	0.0147	7	0.6514	0.0033	3	0.2320	0.0014
4	9	0.0853	0.0216	9	0.2598	0.0048	4	0.0400	0.0009
5	11	0.0226	0.0498	11	0.0822	0.0103	5	0.0109	0.0033
6	13	0.0084	0.0767	13	0.0213	0.0145	6	0.0048	0.0013
7	15	0.0036	0.0347	15	0.0109	0.0055	7	0.0017	0.0008
8	17	0.0009	0.0365	17	0.0089	0.0092	8	0.0004	0.0009

3.10. Effect of Frequency-Point Selection

The approximation methods considered in this study employ different strategies for selecting frequency sampling points. Matsuda and curve-fitting methods use logarithmically distributed frequency samples across the approximation band, with the number of selected points increasing with approximation order. For an n-th order Matsuda approximation, $2n+1$ frequency points are required to construct the continued-fraction interpolation model, while the curve-fitting approach adopts the same logarithmic sampling density for consistency. In contrast, the M-SBL method directly constructs the approximation using only n logarithmically distributed frequency points, resulting in reduced sampling requirements.

The number of frequency points was systematically varied for each method while preserving the same approximation bandwidth. Table 11 shows that increasing the number of selected frequency points generally improves approximation accuracy, as reflected by the reduction in RMSE_m. Matsuda benefits significantly from additional interpolation points due to improved recursive fitting accuracy, although this improvement is accompanied by increased computational cost. The trade-off between approximation accuracy and execution time is further illustrated in Figure 13.

The curve-fitting method also improves with increased sampling density but generally requires a larger number of frequency points to achieve accuracy comparable to Matsuda and M-SBL. This behavior suggests reduced efficiency for broadband approximation. Among the evaluated methods, M-SBL exhibits the most favorable accuracy-to-complexity trade-off. Despite using fewer frequency points, it achieves lower approximation error with consistently low execution time. These results indicate that M-SBL is less sensitive to sampling density while maintaining high approximation fidelity.

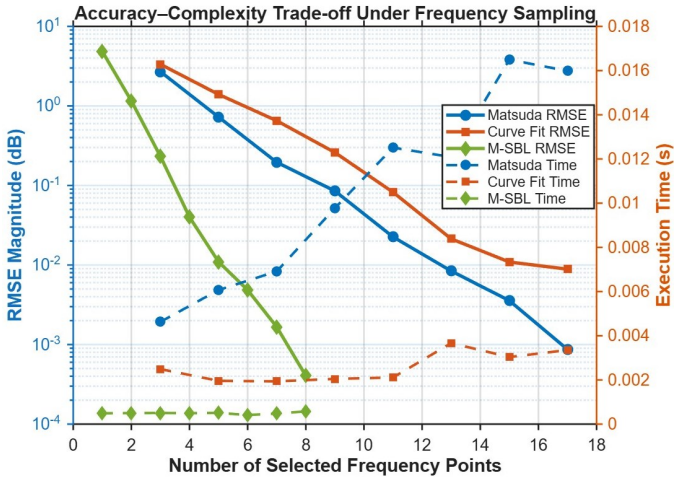


Figure 13. Influence of frequency-point selection on approximation accuracy and computational cost for the fractional operator $G(s) = s^{0.5}$ using Matsuda, curve-fitting, and M-SBL methods.

3.11. Equal-Ripple Biquadratic Approximation for Fractional-Order Integrators and Differentiators

The continued fraction expansion method can be used to derive low-order rational approximations of fractional operators. For a second-order truncation, the resulting model takes the form of a biquadratic transfer function:

$$s^{\alpha} \approx \frac{a_0 s^2 + a_1 s + a_2}{a_2 s^2 + a_1 s + a_0}, \tag{86}$$

where

$$a_0 = \alpha^2 + 3\alpha + 2, \quad a_1 = -2\alpha^2 + 8, \quad a_2 = \alpha^2 - 3\alpha + 2.$$

Similarly, the fractional integrator is obtained as

$$s^{-\alpha} \approx \frac{a_2 s^2 + a_1 s + a_0}{a_0 s^2 + a_1 s + a_2}. \tag{87}$$

Although these models are compact and computationally efficient, they typically exhibit non-uniform approximation errors, resulting in ripple-like deviations in both magnitude and phase responses. To address this issue, ref. [34] introduced an equal-ripple design by incorporating a tuning parameter β into the middle coefficient. The modified transfer function is given by [35]

$$H_d(s) = \frac{(\alpha^2 + 3\alpha + 2)s^2 + (\beta(1 - \alpha^2) + 6)s + (\alpha^2 - 3\alpha + 2)}{(\alpha^2 - 3\alpha + 2)s^2 + (\beta(1 - \alpha^2) + 6)s + (\alpha^2 + 3\alpha + 2)}. \tag{88}$$

The parameter β controls the distribution of approximation error. Increasing β reduces outer ripple at the expense of inner ripple, while decreasing it produces the opposite effect. For each value of α, an optimal β exists that equalizes these ripples, resulting in a minimax approximation. For example, for $\alpha = 0.5$, the optimal value is approximately $\beta \approx 3.8382$, which significantly reduces both magnitude and phase errors [35,41]. To ensure stability, the parameter must satisfy

$$\beta > \frac{1 - \alpha^2}{6}. \tag{89}$$

3.12. Exact-Phase Biquad Approximation for Fractional-Order Integrators

Fractional-order integrators $s^{-\alpha}$ exhibit an ideal constant phase of $-\alpha \times 90°$, which cannot be exactly realized using finite-dimensional systems. A practical approach is to approximate them using a second-order biquadratic structure:

$$H(s) \approx s^{-\alpha} \approx \frac{a_2 s^2 + a_1 s + a_0}{a_0 s^2 + a_1 s + a_2}. \tag{90}$$

This symmetric structure ensures stability and facilitates implementation. The approximation is typically normalized such that $H(j\omega_0) = 1$ at a selected center frequency ω_0, around which both magnitude and phase characteristics are shaped. The exact-phase design strategy enforces zero phase error at ω_0, ensuring that the approximation matches the ideal phase exactly at that frequency. The remaining parameters are then adjusted to maintain phase flatness over a desired range.

According to [35], the coefficients can be expressed as

$$a_0 = \beta_1 + \beta_2 \alpha^v + (\beta_1 + \beta_2)\alpha, \tag{91}$$

$$a_2 = \beta_1 + \beta_2 \alpha^v - (\beta_1 + \beta_2)\alpha, \tag{92}$$

where β_1, β_2, and v are design parameters controlling bandwidth and accuracy.

The middle coefficient is obtained from the phase-matching condition:

$$\text{phase_term} = \tan\left(\frac{(2+\alpha)\pi}{4}\right), \tag{93}$$

$$a_1 = (a_2 - a_0)\,\text{phase_term}. \tag{94}$$

This formulation guarantees exact phase matching at the chosen frequency while allowing controlled shaping of the approximation over the surrounding frequency range. The frequency-domain performance of the exact-phase and equal-ripple biquad approximations is illustrated in Figure 14. The comparison highlights the improved phase consistency achieved by the exact-phase design over the selected frequency band.

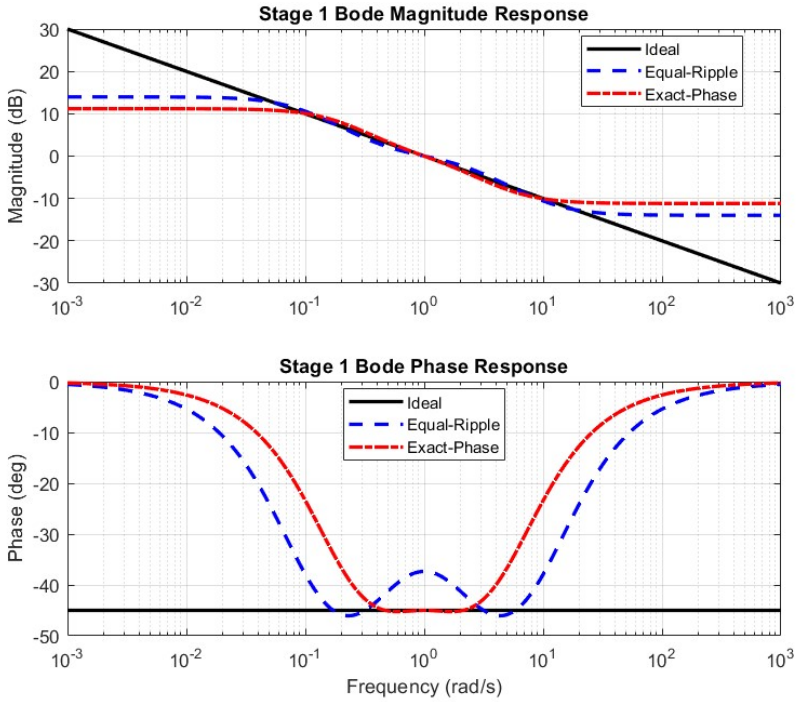


Figure 14. Bode plot of two biquad approximations for a 0.5 order integrator: the exact-phase design (red) vs. an equal-ripple design (blue). The exact-phase biquad achieves a near-constant 45° phase over its band, whereas the ripple-optimized design shows larger phase variation. Both have similar -20×0.5 dB/decade gain slopes, but the exact-phase filter has smoother phase.

Figure 15 presents the Bode plots of equal-ripple and exact-phase approximations for $s^{-0.5}$ using different cascade stages. The results demonstrate the influence of the cascade order on the magnitude and phase approximation accuracy.

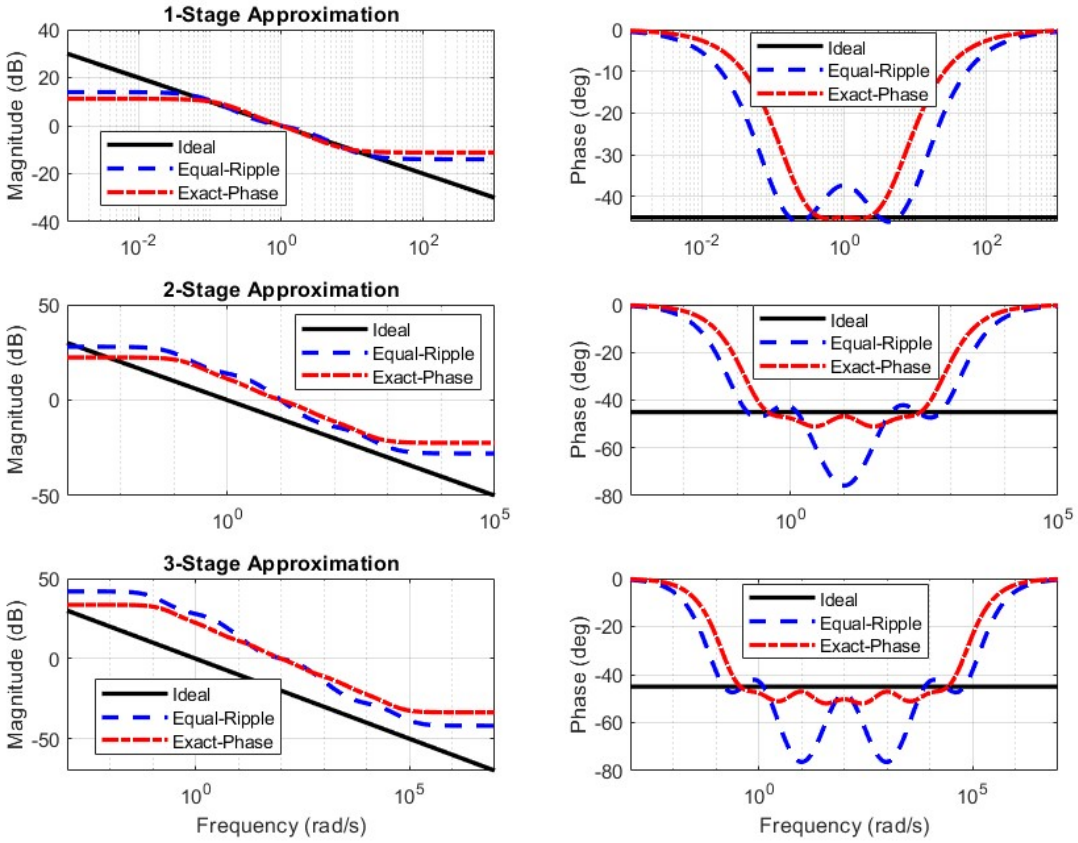


Figure 15. Bode plots of equal-ripple and exact-phase approximations for $s^{-0.5}$ using different cascade stages. The plots compare the accuracy of the magnitude and phase responses of each approximation method against the ideal fractional-order behavior.

The corresponding transfer functions of the equal-ripple and exact-phase approximation methods for different cascade stages are summarized in Table 12.

Table 12. Transfer Functions of Equal-Ripple and Exact-Phase Approximations for $s^{-0.5}$ at Different Stages.

N	Equal-Ripple Transfer Function	Exact-Phase Transfer Function
1	$s^{-0.5} \approx \frac{0.75\,s^2+8.8787\,s+3.75}{3.75\,s^2+8.8787\,s+0.75}$	$s^{-0.5} \approx \frac{0.7613\,s^2+4.8284\,s+2.7613}{2.7613\,s^2+4.8284\,s+0.7613}$
2	$s^{-0.5} \approx \frac{5.625\times10^{-5}\,s^4+0.0673\,s^3+3.6011\,s^2+33.6279\,s+14.0625}{0.0014\,s^4+0.3363\,s^3+3.6011\,s^2+6.7256\,s+0.5625}$	$s^{-0.5} \approx \frac{5.7965\times10^{-5}\,s^4+0.0371\,s^3+2.3357\,s^2+13.4663\,s+7.625}{7.625\times10^{-4}\,s^4+0.1347\,s^3+2.3357\,s^2+3.7129\,s+0.5796}$
3	$s^{-0.5} \approx \frac{5.7965\times10^{-5}\,s^4+0.0371\,s^3+2.3357\,s^2+13.4663\,s+7.625}{7.625\times10^{-4}\,s^4+0.1347\,s^3+2.3357\,s^2+3.7129\,s+0.5796}$	$s^{-0.5} \approx \frac{4.4\times10^{-13}\,s^6+2.8\times10^{-8}\,s^5+1.8\times10^{-4}\,s^4+0.1\,s^3+6.5\,s^2+37.2\,s+21.05}{2.1\times10^{-11}\,s^6+3.7\times10^{-7}\,s^5+6.5\times10^{-4}\,s^4+0.1\,s^3+1.8\,s^2+2.8\,s+0.4}$

3.13. Impulse- and Step-Response-Invariant Discretization Methods

In addition to continuous-time rational approximation methods, discrete-time realization techniques have also been developed for fractional-order operators. Among these approaches, impulse-response-invariant (IRI) and step-response-invariant (SRI) discretization methods proposed by Chen provide finite-dimensional z-domain approximations that preserve the time-domain characteristics of fractional-order integrators and differentiators [42–44].

For a fractional-order operator

$$G(s) = s^r, \qquad -1 < r < 1,$$

where $r > 0$ corresponds to a fractional differentiator and $r < 0$ corresponds to a fractional integrator, the objective is to construct a discrete-time transfer function of the form

$$G(z) = \frac{b_0 + b_1 z^{-1} + \cdots + b_n z^{-n}}{1 + a_1 z^{-1} + \cdots + a_n z^{-n}},$$

where n denotes the approximation order and T_s is the sampling period.

3.13.1. Impulse-Response-Invariant (IRI) Discretization

The impulse-response-invariant method preserves the sampled impulse response of the continuous-time fractional operator. For a fractional integrator

$$G(s) = \frac{1}{s^r}, \qquad 0 < r < 1,$$

the continuous-time impulse response is given by

$$h(t) = \mathcal{L}^{-1}\left\{\frac{1}{s^r}\right\} = \frac{t^{r-1}}{\Gamma(r)},$$

where $\Gamma(\cdot)$ denotes the Gamma function.

Sampling this response using sampling period T_s yields

$$h[k] = h(kT_s) = \frac{(kT_s)^{r-1}}{\Gamma(r)}, \qquad k = 1, 2, \ldots$$

The sampled impulse response sequence is then approximated by a finite-order discrete transfer function through model fitting techniques such as Prony approximation:

$$[b(z), a(z)] = \text{Prony}(h[k]).$$

The resulting discrete approximation becomes

$$G_{\text{IRI}}(z) = \frac{B(z)}{A(z)}.$$

For a fractional differentiator s^r, the inverse relation is used:

$$s^r \approx \frac{1}{G_{\text{IRI}}(z)}.$$

3.13.2. Step-Response-Invariant (SRI) Discretization

The step-response-invariant method preserves the sampled step response of the fractional operator. For a fractional integrator

$$G(s) = \frac{1}{s^r},$$

the continuous-time step response is

$$y(t) = \mathcal{L}^{-1}\left\{\frac{1}{s^{r+1}}\right\} = \frac{t^r}{\Gamma(r+1)}.$$

Sampling the response at interval T_s gives

$$y[k] = y(kT_s) = \frac{(kT_s)^r}{\Gamma(r+1)}, \qquad k = 0, 1, 2, \ldots$$

The sampled step-response sequence is fitted to a discrete transfer function using recursive identification methods such as Steiglitz–McBride iteration:

$$[b(z), a(z)] = \text{STMCB}(y[k]).$$

Thus, the discrete approximation is obtained as

$$G_{\text{SRI}}(z) = \frac{B(z)}{A(z)}.$$

Using the step-response-invariant discretization method with sampling period $T_s = 0.01$ s and approximation order $n = 5$, the fractional-order integrator $s^{-0.5}$ was approximated in the discrete domain as

$$G(s) = s^{-0.5} \approx G_z(z) = \frac{8.8663(z-0.9976)(z-0.9760)(z-0.9089)(z-0.6927)(z-0.0960)}{(z+2.111\times10^{-5})(z-0.4788)(z-0.8336)(z-0.9515)(z-0.9901)} \tag{95}$$

The obtained model preserves the step-response characteristics of the continuous fractional integrator while maintaining stability and minimum-phase behavior in the discrete-time domain, as shown in Figure 16.

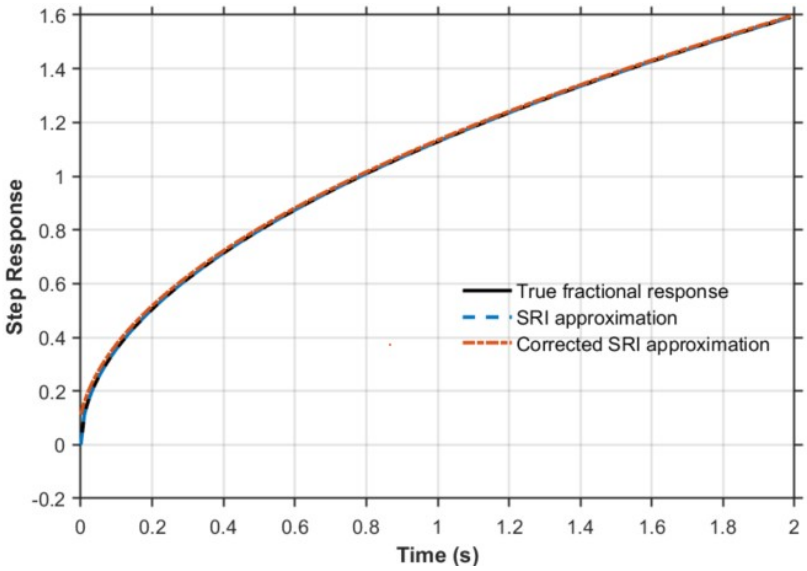


Figure 16. Step-Response-Invariant Approximation of $s^{-0.5}$.

3.13.3. Stability and Minimum-Phase Correction

The identified discrete models may contain unstable poles or nonminimum-phase zeros. Stability correction is typically performed by reflecting poles outside the unit circle:

$$p_i \to \frac{1}{p_i}, \qquad |p_i| > 1,$$

while nonminimum-phase zeros are corrected similarly:

$$z_i \to \frac{1}{z_i}, \qquad |z_i| > 1.$$

These transformations ensure that the resulting approximation remains stable and suitable for digital implementation.

3.14. De Keyser Frequency-Domain Approximation Method

The De Keyser (RDK) approximation method, originally developed by Robin De Keyser and his team [45], provides a discrete-time rational representation of a non-rational fractional-order operator by matching its frequency response over a prescribed frequency interval. Unlike recursive pole-zero approaches, the RDK method constructs the approximation directly from sampled frequency-domain data and converts it into a rational discrete-time transfer function through impulse-response fitting.

The method can be applied to a broad class of non-rational transfer functions, represented as $G_{\mathrm{NRTF}}(s)$, where $G_{\mathrm{NRTF}}(s)$ may include fractional powers, irrational dynamics, or other non-rational operators.

The objective is to determine a rational discrete-time transfer function of order N in the form

$$G_{\mathrm{RDK}}(z^{-1}) = \frac{b_0 + b_1 z^{-1} + b_2 z^{-2} + \cdots + b_N z^{-N}}{1 + a_1 z^{-1} + a_2 z^{-2} + \cdots + a_N z^{-N}}, \tag{96}$$

where a_i and b_i denote the denominator and numerator coefficients obtained through system identification. The denominator is normalized such that its leading coefficient equals unity.

The approximation begins by discretizing the continuous Laplace operator using a generalized generating function that interpolates between Euler and Tustin discretization:

$$s_{\mathrm{RDK}}(z^{-1}) = \frac{1+\alpha}{T}\frac{1 - z^{-1}}{1 + \alpha z^{-1}}, \qquad 0 \le \alpha \le 1, \tag{97}$$

where T is the sampling period, and α is a tuning parameter that controls the high-frequency approximation behavior. The limiting cases correspond to $\alpha = 0$, which yields the Euler discretization, and $\alpha = 1$, which yields the Tustin discretization.

The sampling period is selected according to the maximum approximation frequency $\Omega_{\max}$:

$$T = \frac{\pi}{\Omega_{\max}}, \tag{98}$$

which ensures that $\Omega_{\max}$ corresponds to the Nyquist frequency.

A discrete frequency grid is then generated as

$$\omega_k = \frac{2\pi}{N_s T} k, \qquad k = 0, 1, \ldots, \frac{N_s}{2}, \tag{99}$$

where N_s denotes the number of frequency samples. The associated backward-shift operator is defined by

$$q_k = e^{-j\omega_k T} = z^{-1}. \tag{100}$$

Using the generalized mapping in (97), the frequency response of the non-rational transfer function is evaluated as

$$G[k] = G_{\mathrm{NRTF}}(s_{\mathrm{RDK}}(q_k)), \qquad k = 0, 1, \ldots, \frac{N_s}{2}. \tag{101}$$

To guarantee a real-valued impulse response, conjugate symmetry is imposed:

$$G[N_s - k] = G^*[k], \qquad k = 1, 2, \ldots, \frac{N_s}{2} - 1, \tag{102}$$

where $(\cdot)^*$ denotes complex conjugation.

The impulse response is then computed using the inverse fast Fourier transform (IFFT):

$$g[n] = \frac{1}{N_s} \sum_{k=0}^{N_s-1} G[k] e^{j2\pi kn/N_s}, \qquad n = 0, 1, \ldots, N_s - 1. \tag{103}$$

Finally, the Steiglitz–McBride (STMCB) algorithm is employed to identify a rational discrete-time model from the impulse response:

$$[a_i, b_i] = \mathrm{STMCB}(g[n], N), \tag{104}$$

which yields the rational approximation given in (96).

Therefore, the RDK method transforms the approximation of a non-rational fractional-order operator into a discrete-time identification problem. The approximation order N, maximum frequency $\Omega_{\max}$, and tuning parameter α can be selected independently to balance approximation accuracy and computational complexity.

In this study, the method is demonstrated using the fractional-order low-pass filter

$$G(s) = \frac{1}{(1 + 5s)^{0.5}}. \tag{105}$$

The resulting approximation is expressed in the form. For the selected parameters $N = 4$, $\alpha = 0.9$, and $\Omega_{\max} = 100$ rad/s, the RDK approximation produced the following discrete-time rational transfer function:

$$G_{\mathrm{RDK}}(z^{-1}) = \frac{0.05741 - 0.08132z^{-1} - 0.00855z^{-2} + 0.04283z^{-3} - 0.01017z^{-4}}{1 - 2.363z^{-1} + 1.598z^{-2} - 0.08096z^{-3} - 0.1539z^{-4}}, \tag{106}$$

where z^{-1} denotes the backward-shift operator. The obtained model corresponds to a discrete-time system with sampling period, $T = 0.031416$ s.

Equation (106) represents the fourth-order rational approximation of the fractional-order low-pass filter defined in (105). The approximation preserves the dominant magnitude and phase characteristics of the original fractional-order dynamics over the selected frequency range.

Figure 17 compares the frequency response of the original fractional-order system and the resulting RDK approximation.

The results demonstrate that the RDK method preserves the frequency-domain characteristics of the original fractional-order system over the selected approximation interval while maintaining a low-order rational discrete-time realization.

Unlike frequency-domain approximation techniques such as Oustaloup recursive approximation, Matsuda interpolation, curve-fitting, and M-SBL, the IRI, SRI, and RDK methods are formulated directly in the discrete-time domain. Their approximation accuracy depends not only on the approximation order but also on the sampling period T_s. Consequently, these approaches are particularly attractive for sampled-data control systems and embedded implementation of fractional-order operators. Due to their discrete-time formulation, IRI, SRI, and RDK were not included in the primary Pareto comparison.

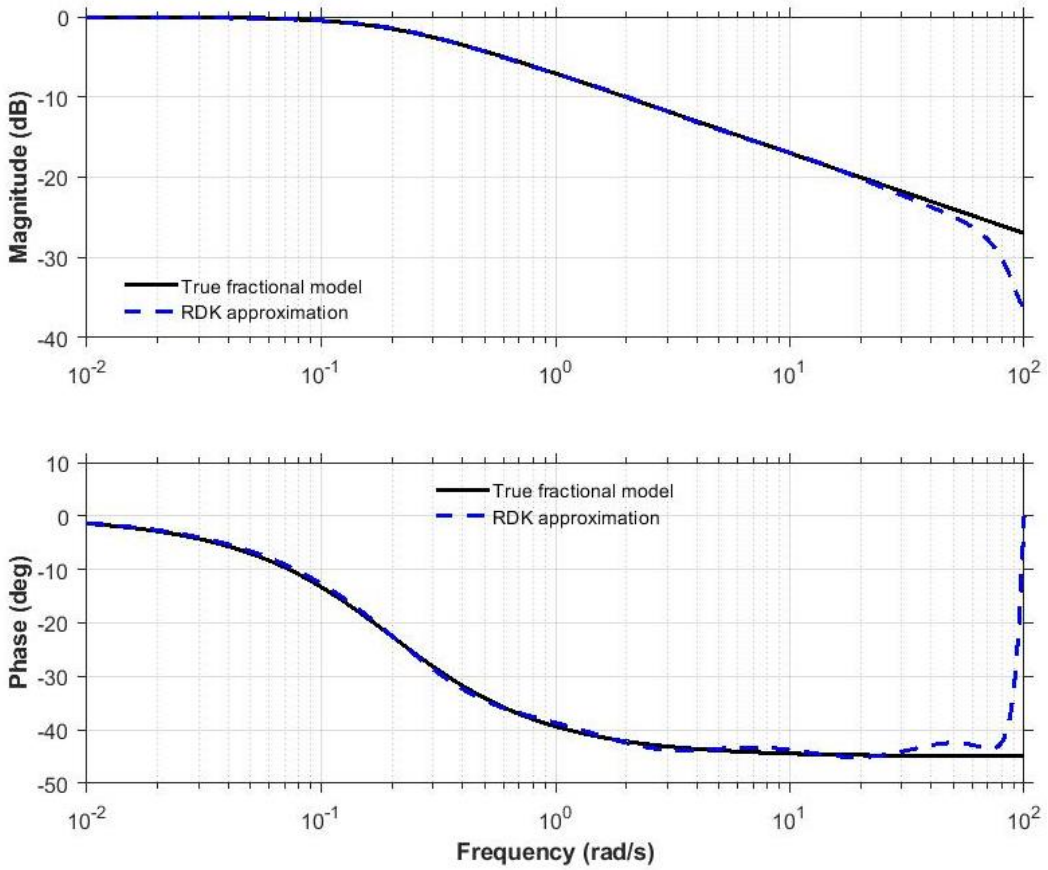


Figure 17. Frequency-response comparison between the original fractional-order system and the RDK discrete-time approximation.

3.15. Genetic Algorithm-Based Fitting Methods

Genetic algorithm (GA)-based fitting methods formulate the approximation of fractional-order operators as an optimization problem; this method of approximation methods is mainly discussed in the literature [46–48]. For a fractional operator $G(s) = s^{\alpha}$, the approximating rational model may be expressed as

$$G_{\mathrm{GA}}(s) = K\frac{\prod_{i=1}^{n}(s+z_i)}{\prod_{i=1}^{n}(s+p_i)}, \tag{107}$$

where K, z_i, and p_i denote the gain, zeros, and poles to be optimized. The optimization process searches for a rational transfer function whose frequency response best matches the target fractional operator over a specified bandwidth.

The optimization objective is commonly defined through a weighted error function:

$$J_{\mathrm{GA}} = w_m\sqrt{\frac{1}{N_\omega}\sum_{k=1}^{N_\omega}\left(M_k-\hat{M}_k\right)^2} + w_p\sqrt{\frac{1}{N_\omega}\sum_{k=1}^{N_\omega}\left(\phi_k-\hat{\phi}_k\right)^2}, \tag{108}$$

where M_k and ϕ_k represent the magnitude and phase responses of the fractional operator, while $\hat{M}_k$ and $\hat{\phi}_k$ correspond to the responses of the approximated rational model. The weighting coefficients w_m and w_p control the relative importance of magnitude and phase matching.

The performance of GA-based fitting methods strongly depends on optimization parameters such as population size, mutation probability, crossover strategy, parameter bounds, and stopping criteria. Therefore, these methods were not included in the main benchmarking framework of this study to maintain deterministic reproducibility across all the compared techniques.

4. Comparative Evaluation Framework and Methodology

This section presents a unified and systematic framework for the comparative evaluation of fractional-order approximation methods. The proposed framework integrates multiple performance criteria, a consistent simulation setup, robustness analysis under frequency-band variation, and a Pareto-based multi-objective decision strategy. This structure ensures a rigorous, reproducible, and application-oriented assessment.

4.1. Performance Evaluation Criteria

The approximation methods are evaluated using a set of complementary criteria that capture both theoretical fidelity and practical implementation aspects. The frequency-domain precision is quantified using the root mean square error in magnitude (RMSE_m) and phase (RMSE_p), along with the corresponding maximum absolute errors. Time-domain performance is assessed using the integral absolute error (IAE) and integral squared error (ISE), which measure the deviation of the approximated response from the ideal fractional-order behavior. Structural complexity is characterized by the number of poles and zeros of the resulting rational model, which directly influences computational burden, numerical conditioning, and implementation feasibility. Stability is evaluated using the classical pole-location criterion, where a model is considered stable if all poles satisfy $\Re(p_i) < 0$. Robustness is assessed by examining the sensitivity of approximation accuracy to variations in the frequency band. This is quantified using the mean and standard deviation of RMSE_m across multiple frequency intervals. These criteria collectively define a multi-objective evaluation problem, where improvements in one metric may lead to degradation in others, necessitating a balanced and systematic comparison.

4.2. Simulation Setup

To ensure a fair and consistent comparison, all approximation methods are evaluated under identical conditions. The benchmark system considered in this study is the fractional-order operator

$$G(s) = s^{\alpha}, \quad \alpha = 0.5, \tag{109}$$

which represents both fractional differentiation and integration commonly encountered in control applications.

The approximation objective is defined as

$$G_{\mathrm{apx}}(j\omega) \approx G(j\omega), \quad \omega \in [\omega_L, \omega_H]. \tag{110}$$

All methods are implemented with the same approximation order ($N = 4$) and evaluated over multiple frequency bands:

$$[\omega_L, \omega_H] \in \left\{ [10^{-3}, 10^{3}],\ [10^{-2}, 10^{2}],\ [10^{-1}, 10^{1}] \right\}. \tag{111}$$

This setup enables a consistent comparison of accuracy, robustness, and complexity across different approximation techniques.

4.3. Robustness Analysis Under Band Variation

The performance of fractional-order approximation methods depends on the selected frequency interval. Accordingly, robustness is assessed by examining how approximation accuracy varies over different frequency bands.

Definition 1 (**Robustness under band variation**). *Let* $\mathrm{RMSE}_m^{(i)}$ *denote the magnitude error associated with the i-th frequency band. The robustness indicators are defined as*

$$\mu = \frac{1}{K}\sum_{i=1}^{K}\mathrm{RMSE}_m^{(i)}, \tag{112}$$

$$\sigma = \sqrt{\frac{1}{K}\sum_{i=1}^{K}\left(\mathrm{RMSE}_m^{(i)} - \mu\right)^2}, \tag{113}$$

where μ *denotes the mean approximation error, and* σ *quantifies sensitivity to band variation.*

Lemma 1 (**Robustness criterion**). *An approximation method is considered robust when both* μ *and* σ *remain sufficiently small.*

Justification. A small μ indicates consistently low approximation error, whereas a small σ reflects weak dependence on the selected frequency interval. By contrast, large variations in $\mathrm{RMSE}_m^{(i)}$ indicate strong band dependence and reduced reliability in practical applications.

4.4. Multi-Objective Selection Framework

The selection of an appropriate approximation method is inherently a multi-objective decision problem and depends on application-specific requirements. In particular, a trade-off exists among frequency-domain accuracy (RMSE_m, RMSE_p), time-domain performance (IAE, ISE), structural complexity (number of poles and zeros), robustness (measured by σ), and computational effort. Methods with higher approximation accuracy often require increased model complexity, whereas simpler models generally sacrifice precision.

Definition 2 (Method selection problem). *Let* $\mathcal{M} = \{M_1, M_2, \ldots, M_K\}$ *denote the set of candidate methods. Each method is evaluated using a normalized performance vector*

$$\tilde{\mathbf{J}}(M_i) = [\tilde{J}_1(M_i), \tilde{J}_2(M_i), \ldots, \tilde{J}_p(M_i)], \tag{114}$$

where the criteria include $RMSE_m$, $RMSE_p$, *IAE, ISE, number of poles, number of zeros, and the robustness indicator* σ.

Definition 3 (**Optimal method under weighted criteria**). *Given a weighting vector* $\mathbf{w}$ *satisfying* $\sum w_k = 1$, *the optimal method is defined as*

$$M^* = \arg\min_{M_i \in \mathcal{P}} \sum_{k=1}^{p} w_k \tilde{J}_k(M_i), \tag{115}$$

where $\mathcal{P}$ *denotes the Pareto-optimal set.*

Lemma 2 (**Application-dependent optimality**). *The optimal method* M^* *depends on the weighting vector* $\mathbf{w}$ *and therefore varies across applications.*

Proposition 1 (**Practical selection principle**). *The selection process should first identify Pareto-optimal methods and then apply a weighted decision index to determine the final choice.*

4.5. Evaluation Procedure

The proposed multi-objective evaluation procedure is summarized in Algorithm 1. The algorithm combines normalized performance metrics, Pareto-optimal analysis, and weighted decision criteria to identify the most suitable fractional-order approximation method for a given application.

The evaluation considers frequency-domain accuracy, time-domain performance, model complexity, and robustness indicators to ensure a balanced selection process.

Algorithm 1 Multi-objective selection of fractional-order approximation method

1: Compute performance metrics for each method: RMSE_m, RMSE_p, IAE, ISE, number of poles, number of zeros, and robustness indicator
2: Normalize all criteria using min–max scaling
3: Identify Pareto-optimal set $\mathcal{P}$ using dominance analysis
4: Assign weights $\mathbf{w}$ based on application requirements
5: **for** each $M_i \in \mathcal{P}$ **do**
6: Compute decision index $D(M_i) = \sum_{k=1}^{p} w_k \tilde{J}_k(M_i)$
7: **end for**
8: Select optimal method $M^* = \arg\min_{M_i \in \mathcal{P}} D(M_i)$
9: **return** M^*

Pareto-Based Multi-Criteria Evaluation

Because the evaluation criteria are mutually conflicting, a Pareto-based multi-objective framework is employed to identify non-dominated solutions [49]. A method is Pareto-optimal if no other method performs better in all criteria simultaneously. In this study, the criteria include frequency-domain accuracy (RMSE_m, RMSE_p), time-domain performance (IAE, ISE), structural complexity, and robustness.

All performance metrics are normalized to the interval $[0, 1]$. A weighted decision index is then defined as

$$J_i = \sum_{k=1}^{M} w_k \, x_{i,k}^{\mathrm{norm}}, \tag{116}$$

where $x_{i,k}^{\mathrm{norm}}$ is the normalized value of the k-th criterion for method i. Higher weights are assigned to frequency-domain accuracy, robustness, and reduced structural complexity. The final ranking is obtained by selecting the method with the minimum decision index within the Pareto-optimal set.

4.6. Decision Framework

The choice of an approximation method depends on the dominant application requirement. If frequency-domain accuracy is the primary objective, Oustaloup-based methods generally provide superior performance. For robustness under band variation, Matsuda demonstrates more consistent behavior. When reduced structural complexity is required, M-SBL offers a favorable trade-off. Curve-fitting approaches tend to improve time-domain behavior.

When several criteria must be satisfied simultaneously, the Pareto-based framework provides a systematic decision mechanism. Pareto analysis identifies the non-dominated candidates, and the weighted decision index determines the final choice. Figure 18 illustrates the proposed decision framework.

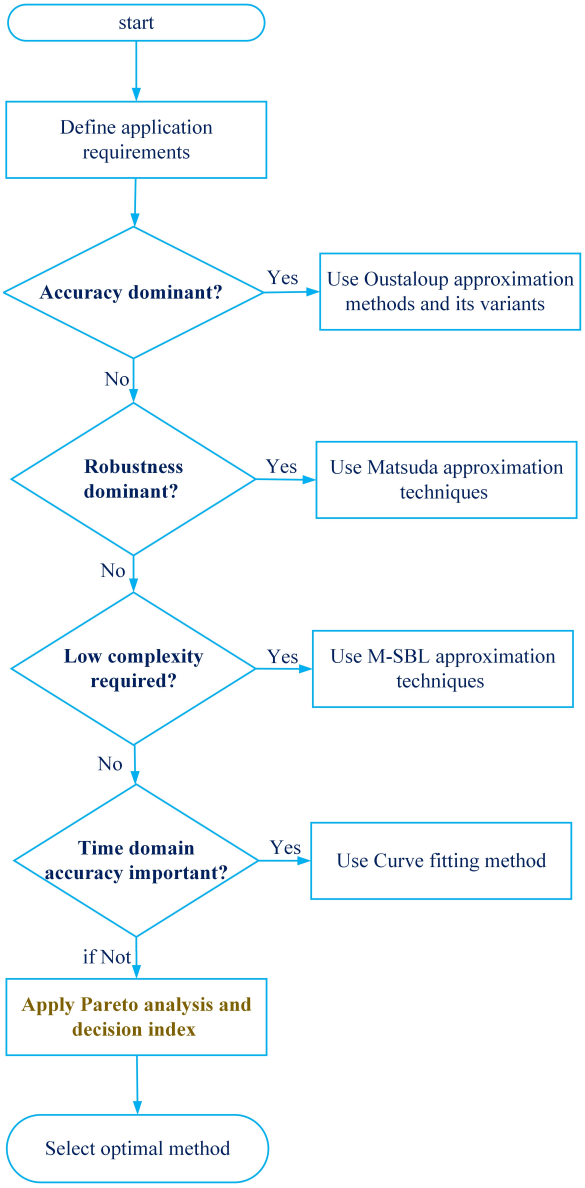


Figure 18. Decision framework for selecting fractional-order approximation methods based on Pareto-optimal trade-offs and application requirements.

5. Results and Discussion

The comparative results summarized in Table 13 highlight the trade-offs among accuracy, robustness, structural complexity, and stability for the considered approximation methods.

Table 13. Performance comparison of approximation methods for $G(s) = s^{0.5}$, including accuracy, robustness, computational complexity, and stability.

Method	Stable	Poles	Zeros	$\max \Re(p)$	T_{exec}	RMSE_m	RMSE_p	Max_m	Max_p	IAE	ISE	μ	σ	J_i	Pareto
ORA	Yes	9	9	−0.003	0.0254	2.98	18.78	10.02	42.34	0.14	0.95	0.10	0.15	0.31	Yes
ROA	Yes	11	11	−0.00045	0.0031	0.93	11.06	4.17	35.86	0.53	10.32	0.45	0.02	0.27	Yes
Matsuda	Yes	4	4	−0.01	0.0154	1.57	16.09	5.28	40.50	0.81	6.82	0.89	0.20	0.22	Yes
Curve-Fit	Yes	4	4	−0.12	0.0175	4.41	22.36	16.15	44.66	0.82	4.81	0.97	0.54	0.29	Yes
M-SBL	Yes	4	4	−0.01	0.0038	2.23	14.71	5.97	38.45	1.16	5.47	1.52	0.50	0.17	Yes
CFE	Yes	4	4	−0.13	0.0133	8.77	30.64	20.92	44.85	0.21	0.46	1.51	2.07	0.36	Yes
El-Khazali-1st	Yes	1	1	−2.41	0.0017	16.82	38.81	32.34	44.99	7.36	3.24	5.95	5.10	0.66	Yes
El-Khazali-2nd	Yes	2	2	−0.62	0.0015	13.81	36.12	28.34	44.97	3.20	1.43	4.06	3.92	0.49	Yes

5.1. Stability Analysis

All approximation methods produce stable integer-order models, as indicated by $\max \Re(p) < 0$ in all cases. However, several models exhibit poles close to the imaginary axis, particularly refined Oustaloup, which may reduce stability margins. This observation indicates that stability alone is insufficient as a selection criterion and should be considered jointly with robustness and numerical conditioning. A detailed discussion of this analysis is provided in Section 5.9.

5.2. Frequency-Domain Accuracy

Refined Oustaloup achieves the lowest RMSE_m and RMSE_p, indicating the highest frequency-domain accuracy. Standard Oustaloup also performs well, although with slightly larger error values. Matsuda and M-SBL provide moderate accuracy with substantially reduced model order. In contrast, CFE and El-Khazali methods exhibit large errors, particularly in phase, indicating weaker approximation fidelity over the selected frequency range.

5.3. Time-Domain Performance

CFE achieves the lowest IAE and ISE values, indicating strong time-domain approximation capability. However, this advantage is obtained at the expense of significantly reduced frequency-domain accuracy. El-Khazali methods show weaker transient performance, especially the first-order variant.

5.4. Structural Complexity

El-Khazali methods provide the lowest structural complexity, followed by Matsuda, M-SBL, Curve Fit, and CFE, each with four poles. Oustaloup-based methods require higher-order realizations, which increases implementation complexity and computational cost.

5.5. Robustness to Frequency Band Variation

Robustness analysis shows that refined Oustaloup achieves the lowest standard deviation ($\sigma = 0.02$), indicating the highest insensitivity to band selection. Standard Oustaloup and Matsuda also exhibit comparatively good robustness, whereas CFE and El-Khazali methods show much larger variability, indicating weaker robustness.

5.6. Multi-Objective Trade-Off Analysis

Fractional-order operator approximation is inherently a multi-objective optimization problem because improving one performance criterion often leads to degradation in another. Increasing approximation order may enhance frequency-domain accuracy while simultaneously increasing computational burden, model complexity, and numerical sensitivity. Consequently, no single approximation method can be considered universally optimal across all performance indicators.

To address this challenge, a Pareto-based framework was adopted to compare competing approximation methods using multiple criteria simultaneously. The evaluated objectives include frequency-domain accuracy, time-domain performance, robustness, structural complexity, and execution time. Similar single-objective formulations have been widely adopted in fractional-order approximation and control design studies [7,12,49].

The generalized multi-objective vector can be written as

$$\mathbf{F}(N) = \left[\mathrm{RMSE}_m, \mathrm{RMSE}_p, \mathrm{IAE}, \mathrm{ISE}, N_p, N_z, \sigma, T_{\mathrm{exec}}\right], \tag{117}$$

where N_p and N_z denote the number of poles and zeros, σ represents robustness variation, and T_{exec} denotes average execution time.

A solution is considered Pareto-optimal when no other candidate improves one objective without degrading at least one remaining objective. Since multiple objectives conflict, Pareto analysis provides a rational framework for selecting approximation methods without relying on a single metric [49,50]. The weighted decision index J_i was introduced as a secondary ranking criterion to identify the most balanced non-dominated solution.

Table 13 indicates that M-SBL achieves the lowest decision index J_i, demonstrating the best overall compromise among approximation accuracy, robustness, structural complexity, and computational effort. Although ROA provides superior frequency-domain fitting performance, its higher model order ($polesandzeros = 11$) increases structural complexity and implementation burden. Matsuda offers a balanced trade-off by combining moderate approximation accuracy with relatively low model order. These observations are further supported by Figures 19 and 20, where M-SBL, Matsuda, and Oustaloup-based approximations consistently appear near the optimal Pareto region. This positioning confirms their suitability as balanced approximation methods capable of maintaining favorable trade-offs across multiple performance objectives.

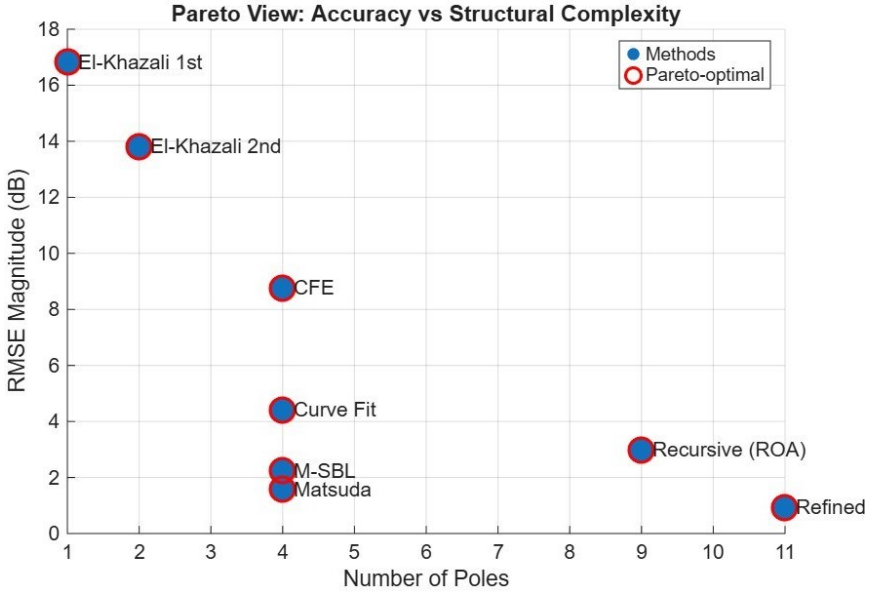


Figure 19. Pareto visualization showing the trade-off between approximation accuracy and structural complexity.

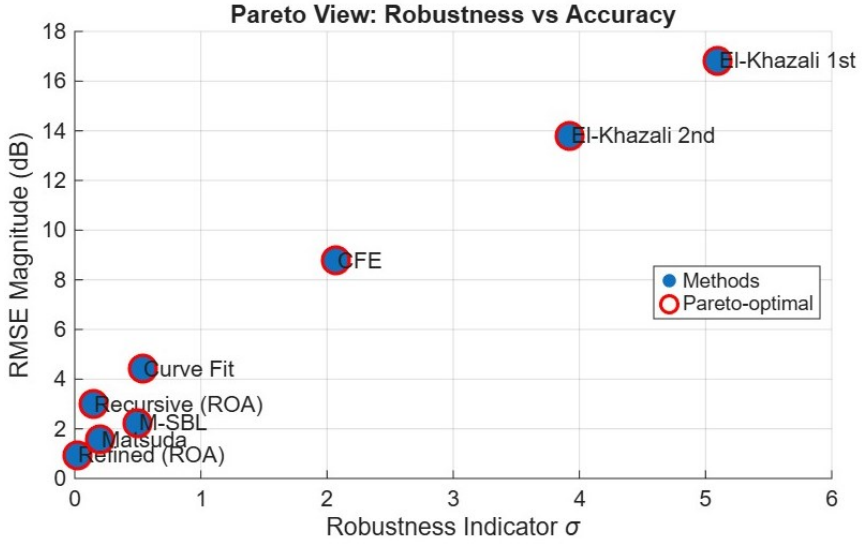


Figure 20. Pareto visualization showing robustness vs. approximation accuracy.

5.7. Pareto Analysis and High-Dimensional Extension

Traditional Pareto analysis is often illustrated through binary trade-off relationships such as accuracy vs. complexity or robustness vs. accuracy. However, Pareto optimization is not restricted to two-dimensional analysis. For three objectives, the Pareto front becomes a surface, whereas for four or more objectives, it becomes a high-dimensional Pareto manifold [49,50]. In the present study, the generalized Pareto representation may be written as

$$\mathbf{F}(N) = [\text{Accuracy}, \text{Robustness}, \text{Complexity},]. \tag{118}$$

In this formulation, accuracy is quantified using RMSE measures, robustness is represented by σ, and complexity is determined from pole-zero count and execution time.

Figure 21 presents a three-dimensional (3-D) Pareto surface for multi-objective evaluation, enabling simultaneous visualization of competing objectives including approximation accuracy, robustness, and structural complexity. Unlike conventional two-dimensional Pareto curves, the 3-D representation provides a more comprehensive interpretation of trade-offs among multiple performance indicators within a unified decision space. The extension from Pareto curves to Pareto surfaces enables simultaneous visualization of more than two conflicting objectives. Such representations are increasingly used in engineering optimization and decision-making problems [49,50].

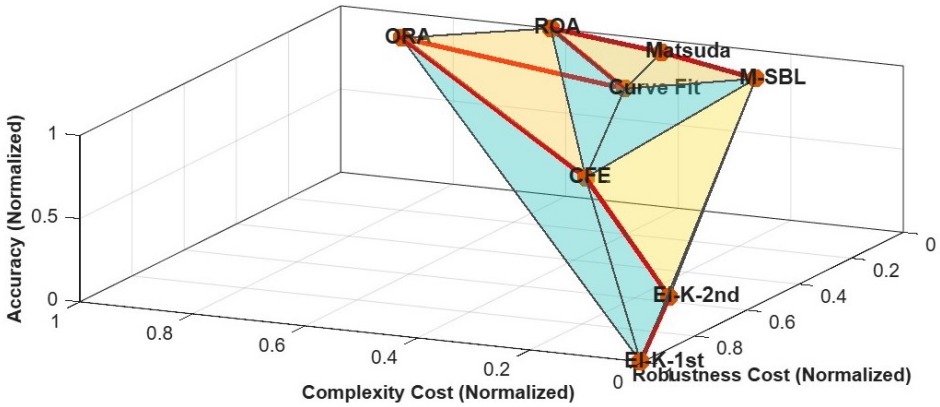


Figure 21. Three-dimensional Pareto surface showing simultaneous optimization of complexity, robustness, and approximation accuracy.

5.8. Optimal Approximation Order Selection

To determine the most suitable approximation order, the order parameter N was varied from 4 to 15 for the selected approximation methods. Based on the Pareto analyses presented in Figures 19 and 20, M-SBL, Matsuda, and Oustaloup-based methods consistently occupy regions close to the Pareto-optimal boundary, indicating favorable trade-offs among approximation accuracy, robustness, structural complexity, and computational effort. Consequently, these methods were further examined through an order-selection analysis. For each approximation order, the decision index J_i was computed using normalized performance metrics derived from frequency-domain accuracy, time-domain error, robustness variation, model complexity, and execution time. To reduce variability associated with computational timing, each approximation was executed over 20 independent runs, and the average execution time was used in the decision-index calculation. The optimal order for each method was then identified as the order corresponding to the minimum average decision index, Min. $J_{i,a}$.

The results in Table 14 and Figure 22 indicate that M-SBL achieved the lowest decision index at $N = 9$, suggesting the best overall compromise among competing objectives. Matsuda reached its optimal performance at $N = 7$, while both ORA and ROA achieved

their best trade-off at $N = 4$. Although curve-fit attained its minimum decision index at $N = 8$, its relatively high J_i value indicates weaker overall performance compared to the other methods. These findings confirm that increasing approximation order does not necessarily improve overall quality and that an optimal order emerges from balancing approximation accuracy, robustness, and computational complexity.

Table 14. Optimal approximation order selected using the Pareto-based decision index for $G(s) = s^{0.5}$.

Method	Optimal N	Min. $J_{i,a}$
ORA	4	0.1876
ROA	4	0.0976
Matsuda	7	0.0998
Curve Fit	8	0.5285
M-SBL	9	0.0704

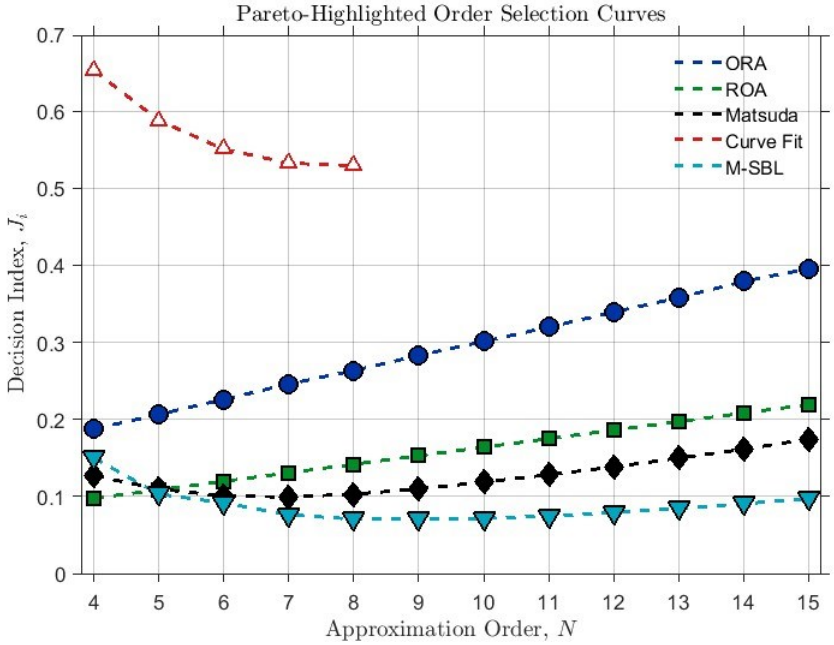


Figure 22. Decision index vs. approximation order for fractional operator $G(s) = s^{0.5}$. Lower values indicate better compromise among accuracy, robustness, and complexity.

For the curve-fit approximation, valid time-domain indices were obtained only up to $N = 8$. Beyond this order, the fitted rational models produced numerically unstable or ill-conditioned transfer functions, resulting in undefined step-response metrics (IAE and ISE). Although frequency-domain fitting remained computable, higher-order curve-fit models exhibited poor numerical robustness during time-domain simulation. This behavior suggests that increasing approximation order does not necessarily improve model quality and may introduce instability due to over-parameterization and pole-zero ill-conditioning.

5.9. Stability Mismatch Between Fractional-Order Models and Their Rational Approximations

Fractional-order systems are commonly approximated by integer-order rational models to enable practical implementation and simulation. However, this approximation process does not necessarily preserve the intrinsic stability properties of the original fractional-order system. As a result, discrepancies between the stability of the fractional model and its approximation may arise. A fractional-order transfer function can be stable under Matignon's criterion, while its integer-order approximation can be unstable. The reverse

situation may also occur. For a commensurate fractional-order system of order q, stability requires [26,51]

$$|\arg(\lambda_i)| > \frac{q\pi}{2}, \tag{119}$$

where λ_i are the roots of the characteristic polynomial expressed in the transformed variable. In contrast, for an integer-order approximation, stability is determined using the classical condition [52]:

$$\Re(p_i) < 0, \tag{120}$$

where p_i are the poles of the approximated system. These two stability criteria are fundamentally different. Consequently, the approximation process may alter pole locations and phase characteristics, which can lead to a change in the stability properties of the system [28].

Case studies:

To illustrate this mismatch, two representative cases are considered. First, a stable fractional-order system that becomes unstable after approximation is considered. The azimuth channel fractional-order transfer function of twin rotor system described in Section 6 is given by

$$G_1(s) = \frac{700.7}{5.14\,s^{2.87} + 3.73\,s^{1.37} + 0.74\,s^{0.08}}. \tag{121}$$

The fractional-order stability region can be analyzed by rewriting the denominator in a commensurate form. A practical choice is $q = 0.01$, since

$$2.87 = 287 \times 0.01, \quad 1.37 = 137 \times 0.01, \quad 0.08 = 8 \times 0.01.$$

By introducing the transformation $\lambda = s^{0.01}$, the characteristic equation becomes

$$5.14\,\lambda^{287} + 3.73\,\lambda^{137} + 0.74\,\lambda^{8} = 0. \tag{122}$$

For a commensurate fractional-order system of order $q = 0.01$, Matignon's stability condition is given by

$$|\arg(\lambda_i)| > \frac{q\pi}{2} = 0.9^\circ. \tag{123}$$

The original fractional-order transfer function is stable according to Matignon's criterion, as illustrated in Figure 23, where all poles lie outside the shaded instability sector upon zoom in. However, its refined Oustaloup approximation, obtained over the frequency band $[10^{-2}, 10^{2}]$ with approximation order $N = 4$, results in an unstable integer-order model, demonstrating that stability is not preserved under approximation.

Second, an unstable fractional-order system that appears stable after approximation is considered. The system is given by

$$G_2(s) = \frac{1}{s^{0.5} - 1.2}. \tag{124}$$

The system $G_2(s)$ is unstable according to Matignon's criterion. The characteristic equation $s^{0.5} - 1.2 = 0$ can be expressed in commensurate form with $q = 0.5$ by introducing $\lambda = s^{0.5}$, which yields $\lambda - 1.2 = 0$ with root $\lambda = 1.2$. Since $|\arg(\lambda_i)| > \frac{q\pi}{2} = 45^\circ$ is not satisfied (as $\arg(1.2) = 0^\circ$), the system violates the fractional-order stability condition, as shown in Figure 24. However, its recursive Oustaloup approximation, obtained over the frequency band $[10^{-3}, 10^{3}]$ with approximation order $N = 6$, results in a stable integer-order model. This demonstrates that the approximation process can alter the stability characteristics, leading to an apparent stabilization of an originally unstable fractional-order system.

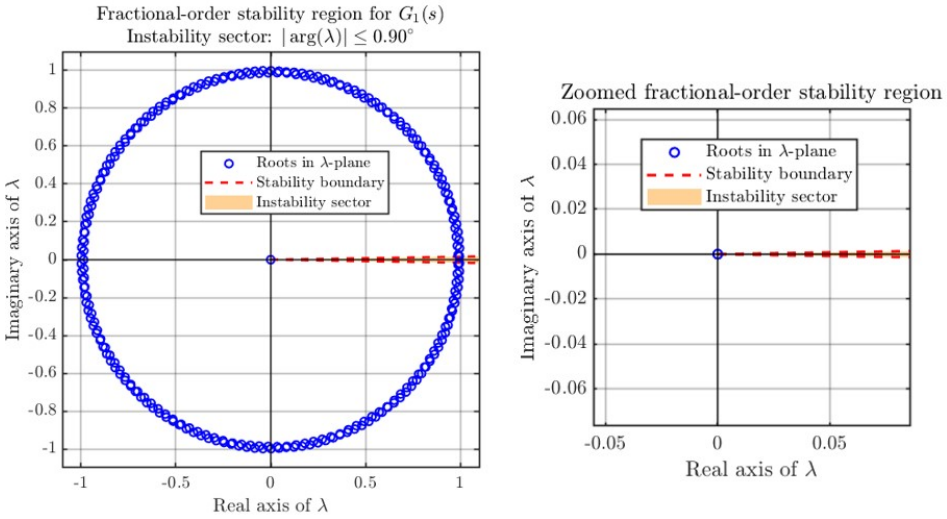


Figure 23. Fractional-order stability region corresponding to (121), showing that all poles lie outside the instability sector.

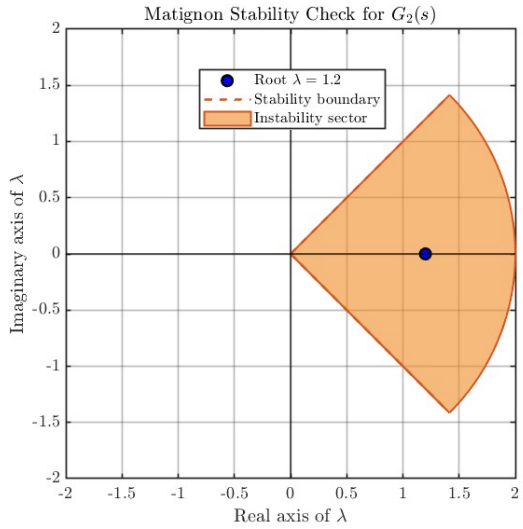


Figure 24. Fractional-order stability region corresponding to (124), showing that one pole lies inside the shaded region.

From the above two cases, it is evident that integer-order approximation does not guarantee the preservation of stability. The choice of approximation method, as well as the selected frequency band and approximation order, plays a critical role in determining the resulting stability properties. In certain cases, the approximation may introduce artificial damping, leading to an apparent stabilization of an originally unstable fractional-order system. Therefore, stability must be verified independently for both the original fractional-order model and its integer-order approximation. The approximation process should be carefully designed, considering the trade-off between approximation accuracy and stability preservation.

6. Illustrative Example and Summary Discussion of Fractional Operator Approximations

The azimuth channel is identified using experimental data obtained from a voltage input in the range of 0–5 V. Based on prior knowledge of the system dynamics, a second-order structure is assumed for the model. Fractional-order model identification is carried out using the MATLAB function `fotfid` from the FOMCON toolbox [53]. In this study,

cross-coupling effects between the azimuth and elevation channels are neglected, which is a reasonable assumption when the elevation rotor is fixed or when coupling effects remain small within the frequency range of interest. Following the identification procedure described in [53], the azimuth dynamics of the TRMS are modeled using both fractional-order and integer-order approaches. The Oustaloup approximation and its refined variant are employed due to their demonstrated accuracy, as discussed earlier in this paper.

The identified fractional-order models are given as

$$G_2(s) = \frac{700.7}{5.1392\, s^{2.8691} + 3.7335\, s^{1.3709} + 0.73496\, s^{0.083266}}, \tag{125}$$

which provides the best fit, with a model fitness of 97.8% using the refined Oustaloup approximation.

$$G_3(s) = \frac{700.7}{5.14\, s^{2.87} + 3.73\, s^{1.37} + 0.74\, s^{0.08}}, \tag{126}$$

yielding a model fitness of 97.32%.

For comparison, the integer-order model reported in [54] is given by

$$G_{\text{int}}(s) = \frac{700.7}{5.61\, s^2 + 3.992\, s + 1}, \tag{127}$$

which achieves a significantly lower model fitness of 91%.

The results indicate that fractional-order models provide a substantially improved representation of the system dynamics compared to the integer-order model. In particular, the refined Oustaloup-based identification yields the highest accuracy, demonstrating its effectiveness in capturing the underlying fractional dynamics of the TRMS. A comparison between the identified models and the experimental data is shown in Figure 25.

All fractional-order approximation techniques were implemented over the frequency range $[\omega_l = 0.01,\ \omega_h = 100]$ rad/s, with an approximation order of $N = 5$, ensuring a consistent basis for comparison.

The corresponding Bode plot of the integer-order approximation for the respective fractional-order system is presented in Figure 26.

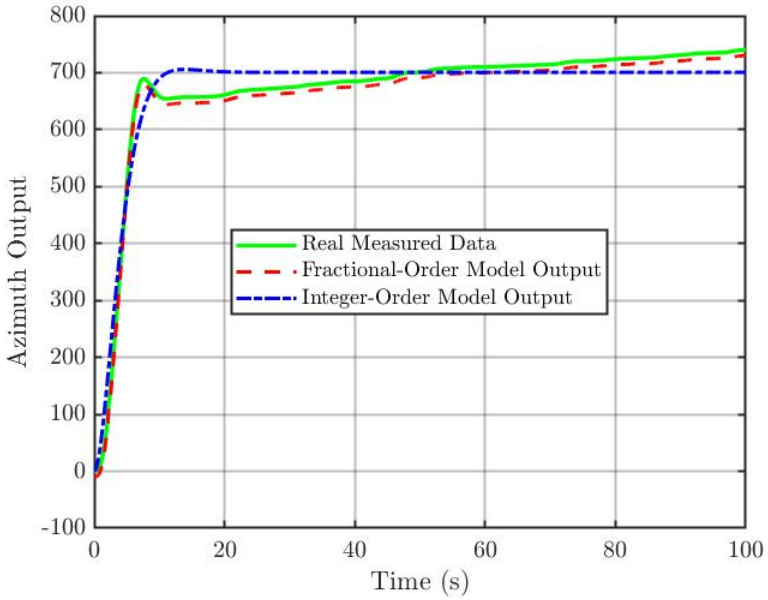


Figure 25. Comparison between fractional-order models identified using the refined Oustaloup approximation and the integer-order model reported in [54].

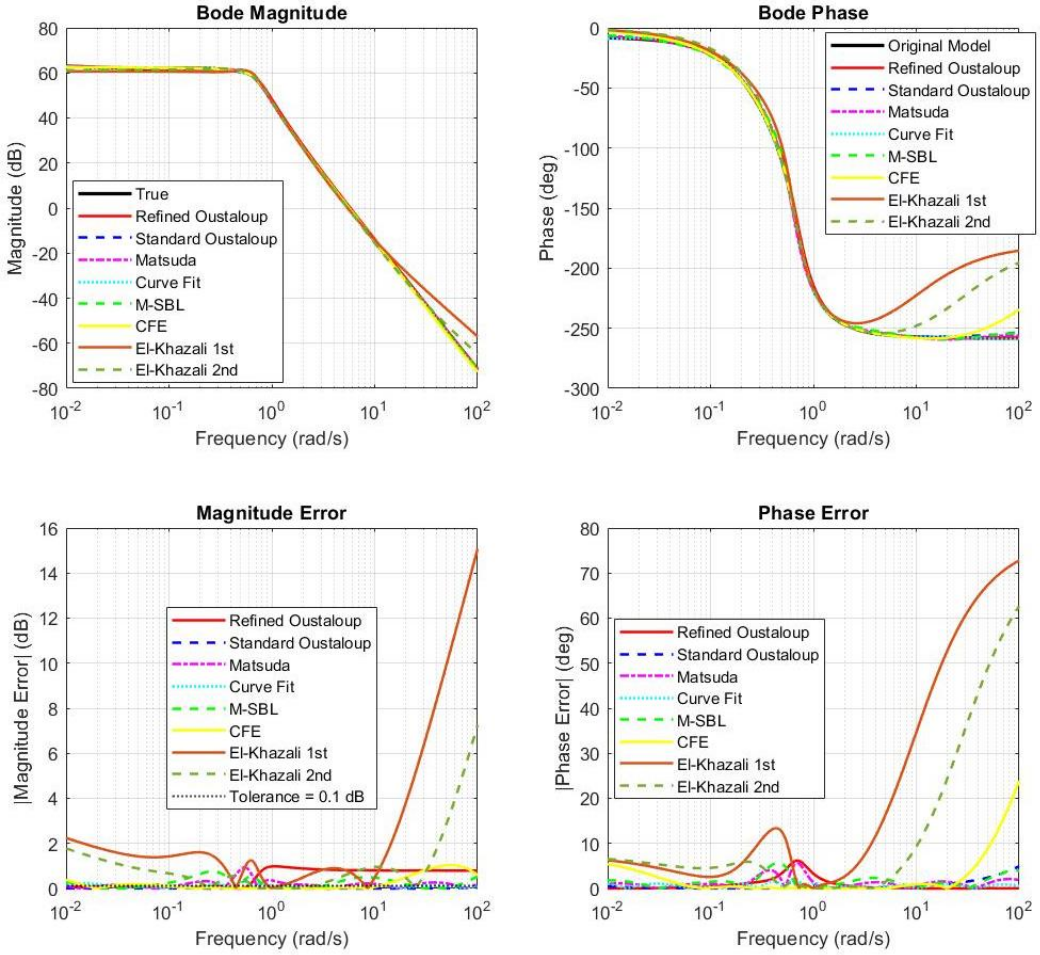


Figure 26. Bode plot comparison of fractional-order approximation methods for the Equation (126) within the frequency range $[0.01, 100]$ rad/s.

The results presented in Table 15 provide a comprehensive comparison of the considered approximation methods in terms of accuracy, stability, and overall performance as quantified by the decision index J_i. From the stability perspective, all methods except the refined Oustaloup approximation exhibit stable behavior, as indicated by negative real parts of the poles. Although the refined Oustaloup method achieves reasonable accuracy, the presence of poles on the imaginary axis suggests marginal stability, which may limit its practical applicability in control systems.

Table 15. Comprehensive performance comparison of approximation methods for the Equation (126) at order 5, including accuracy, robustness, and decision index J_i.

Method	Stable	Poles	$\max \Re(p)$	RMSE_m	RMSE_p	Max_m	Max_p	IAE	ISE	J_i
Refined Oustaloup	No	36	0.001	0.61	1.61	0.98	6.22	382.54	7771.50	0.35
Standard Oustaloup	Yes	32	−0.003	0.01	1.15	0.04	4.90	57.44	136.21	0.28
Matsuda	Yes	16	−0.0001	0.24	1.66	0.94	5.66	437.31	10,232.00	0.23
Curve Fit	Yes	16	−0.01	0.12	0.74	0.30	2.20	137.32	1510.40	0.21
M-SBL	Yes	16	−0.0006	0.31	1.99	0.75	5.71	749.38	35,860.00	0.25
CFE	Yes	14	−0.07	0.38	5.00	1.04	23.89	81.04	563.92	0.20
El-Khazali 1st	Yes	5	−0.18	4.29	31.19	15.07	72.79	5525.70	1.27×10^6	0.74
El-Khazali 2nd	Yes	8	−0.24	1.64	20.45	7.26	62.65	3400.00	5.44×10^5	0.47

In terms of frequency-domain accuracy, the standard Oustaloup method demonstrates superior performance, achieving the lowest magnitude error ($\text{RMSE}_m = 0.01$ dB) and

minimal peak magnitude deviation. However, its phase error remains moderate compared to other methods. The curve fit and Matsuda methods offer a balanced trade-off between magnitude and phase accuracy, with curve fit achieving relatively low phase error and maximum deviation, making it suitable for applications requiring consistent frequency response characteristics. The CFE method stands out in the overall evaluation, yielding the lowest decision index $J_i = 0.20$. Despite moderate magnitude and phase errors, it achieves significantly lower integral error measures (IAE and ISE), indicating improved time-domain performance. Thus, CFE offers a favorable compromise between accuracy and dynamic response, especially for lower frequency control applications. The M-SBL method demonstrates competitive phase accuracy but exhibits relatively high time-domain errors, reflected in larger IAE and ISE values. Similarly, the Matsuda method provides acceptable frequency-domain accuracy but does not achieve the same level of robustness in time-domain performance. In contrast, the El-Khazali approximations (both first- and second-order) exhibit significantly higher errors across most performance metrics, particularly in phase deviation and integral error indices. Although these methods maintain stability and a low model order. Finally, the Pareto analysis confirms that methods such as standard Oustaloup, Matsuda, and M-SBL lie on the optimal trade-off frontier, representing the most efficient balance between competing performance criteria. The step responses of the considered approximation methods are presented in Figure 27, providing a comparative assessment of their time-domain behavior. The results indicate that the Oustaloup method and its variants, along with the Matsuda and CFE approaches, closely match the ideal response, demonstrating superior time-domain performance.

This example highlights the effectiveness of various fractional-order approximation techniques in modeling a real-world nonlinear system. The comparative evaluation using both time- and frequency-domain analyses underscores the trade-offs between model fidelity and complexity. These insights provide a foundation for selecting appropriate approximation methods in fractional-order controller design and system analysis.

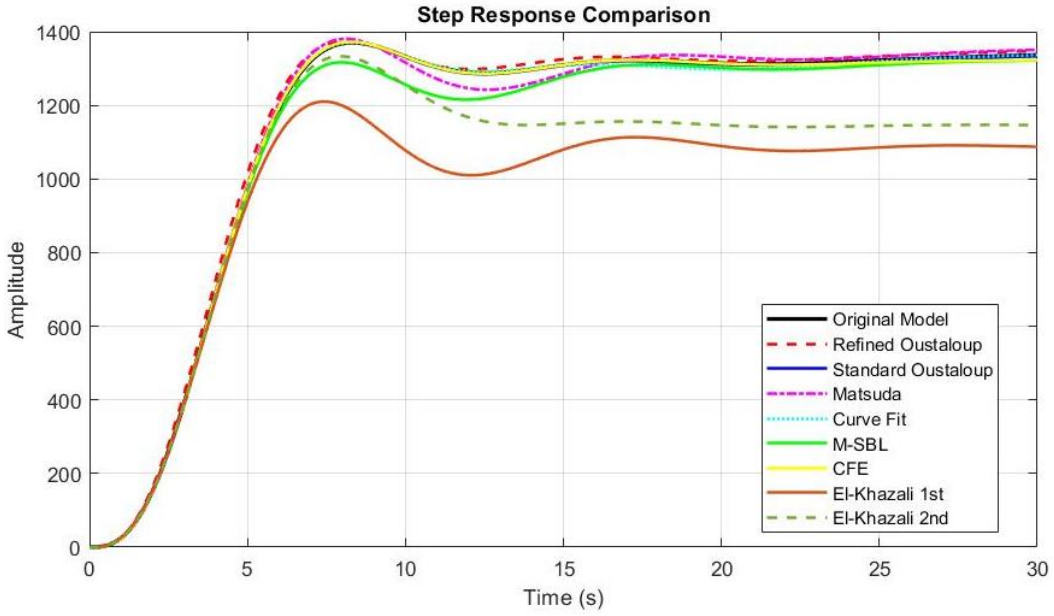


Figure 27. Step response comparison of fractional-order approximation methods for Equation (126).

7. Conclusions

This paper presented a comprehensive evaluation framework for fractional-order operator approximation methods. By integrating multi-objective Pareto analysis, the proposed approach provides deeper insight into the trade-offs among competing performance

criteria. The results demonstrate that no single method is universally optimal; rather, the selection of an appropriate approximation technique depends on specific application requirements. This is further supported through an illustrative example, which highlights the effectiveness of fractional-order operator approximation in a representative dynamic system. Among the evaluated methods, Oustaloup, Matsuda, and M-SBL approaches consistently exhibit strong performance across multiple criteria, while other methods show limitations, particularly over wide frequency ranges. Overall, the proposed framework offers a systematic and practical basis for the selection and evaluation of fractional-order approximation techniques in control applications. Future work will extend the proposed framework to more complex dynamic systems and investigate optimization strategies to improve approximation accuracy, robustness, and computational efficiency. Discrete-time fractional approximations, particularly FOBD and CFE methods, will also be explored as a continuation of this study. In addition, future research will evaluate these approximation methods in closed-loop control applications, including fractional-order PID (FOPID) systems, to assess their impact on rise time, overshoot, settling behavior, and phase margin.

Author Contributions: Conceptualization, A.A.W. and R.M.; methodology, A.A.W. and R.M.; software, A.A.W.; validation, A.A.W. and I.S.; formal analysis, A.A.W. and I.S.; investigation, A.A.W., M.K.W., and M.T.R.; resources, R.M.; writing—original draft preparation, A.A.W.; writing—review and editing, R.M., I.S., and F.T.Y.; visualization, A.A.W., M.T.R., and M.K.W.; supervision, R.M.; project administration, R.M. All authors have read and agreed to the published version of the manuscript.

Funding: This work was supported by the Internal Grant Agency of the Tomas Bata University in Zlín, under the project number IGA/CebiaTech/2024/001.

Data Availability Statement: The data supporting the findings of this study are available from the corresponding author upon reasonable request. The results are based on simulation, numerical analysis, and experimental modeling.

Acknowledgments: The authors acknowledge the support of Tomas Bata University in Zlín for providing the research environment and computational resources.

Conflicts of Interest: The authors declare no conflicts of interest.

References

1. Podlubny, I. Fractional-order systems and $PI^{\lambda}D^{\mu}$ controllers. *IEEE Trans. Autom. Control* **1999**, *44*, 208–214. [CrossRef]
2. Oldham, K.B.; Spanier, J. *The Fractional Calculus*; Academic Press: New York, NY, USA, 1974.
3. Toledo-Hernandez, R.; Rico-Ramirez, V.; Iglesias-Silva, G.A.; Diwekar, U.M. A fractional calculus approach to the dynamic optimization of biological reactive systems. Part I: Fractional models for biological reactions. *Chem. Eng. Sci.* **2014**, *117*, 217–228. [CrossRef]
4. Magin, R.L. Fractional Calculus in Bioengineering. *Crit. Rev. Biomed. Eng.* **2004**, *32*, 1–104. [CrossRef]
5. Monje, C.A.; Chen, Y.Q.; Vinagre, B.M.; Xue, D.; Feliu-Batlle, V. *Fractional-Order Systems and Controls: Fundamentals and Applications*; Springer: London, UK, 2010.
6. Carlson, G.; Halijak, C. Approximation of fractional capacitors $(1/s)^{1/n}$ by a regular Newton process. *IEEE Trans. Circuit Theory* **1964**, *11*, 210–213. [CrossRef]
7. Oustaloup, A.; Levron, F.; Mathieu, B.; Nanot, F.M. Frequency-band complex noninteger differentiator: Characterization and synthesis. *IEEE Trans. Circuits Syst. I Fundam. Theory Appl.* **2000**, *47*, 25–39. [CrossRef]
8. Valério, D.; Sá da Costa, J. Tuning of fractional PID controllers with Ziegler–Nichols-type rules. *Signal Process.* **2006**, *86*, 2771–2784. [CrossRef]
9. Xue, D.; Zhao, C.; Chen, Y.Q. A modified approximation method of fractional-order system. In *Proceedings of the IEEE International Conference on Mechatronics and Automation, Luoyang, China, 25–28 June 2006*; IEEE: New York, NY, USA, 2006; pp. 1043–1048. [CrossRef]
10. Tepljakov, A. *Fractional-Order Modeling and Control of Dynamic Systems*; Springer: Cham, Switzerland, 2017.
11. Zheng, W.; Luo, Y.; Chen, Y.Q.; Pi, Y. Fractional-order modeling of permanent magnet synchronous motor speed servo system. *J. Vib. Control* **2016**, *22*, 2255–2280. [CrossRef]

12. Vinagre, B.M.; Podlubny, I.; Hernandez, A.; Feliu, V. Some approximations of fractional-order operators used in control theory and applications. *Fract. Calc. Appl. Anal.* **2000**, *3*, 231–248.
13. Matsuda, K.; Fujii, H. H_∞ optimized wave-absorbing control: Analytical and experimental results. *J. Guid. Control Dyn.* **1993**, *16*, 1146–1153. [CrossRef] [PubMed]
14. Charef, A.; Sun, H.H.; Tsao, Y.Y.; Onaral, B. Fractal system as represented by singularity function. *IEEE Trans. Autom. Control* **1992**, *37*, 1465–1470. [CrossRef]
15. Bingi, K.; Ibrahim, R.; Karsiti, M.N.; Hassam, S.M.; Harindran, V.R. Frequency response-based curve fitting approximation of fractional-order PID controllers. *Int. J. Appl. Math. Comput. Sci.* **2019**, *29*, 311–326. [CrossRef]
16. Sanathanan, C.; Koerner, J. Transfer function synthesis as a ratio of two complex polynomials. *IEEE Trans. Autom. Control* **1963**, *8*, 56–58. [CrossRef]
17. Deniz, F.N.; Alagoz, B.B.; Tan, N.; Koseoglu, M. Revisiting four approximation methods for fractional-order transfer function implementations. *Annu. Rev. Control* **2020**, *49*, 239–257. [CrossRef]
18. Koseoglu, M.; Deniz, F.N.; Alagoz, B.B.; Alisoy, H. An effective analog circuit design of approximate fractional-order derivative models. *Eng. Sci. Technol. Int. J.* **2022**, *33*, 101069. [CrossRef]
19. Chen, Y.Q.; Petráš, I.; Xue, D. Fractional order control—A tutorial. In *Proceedings of the American Control Conference, St. Louis, MO, USA, 10–12 June 2009*; IEEE: New York, NY, USA, 2009; pp. 1397–1411. [CrossRef]
20. Kapetina, M.N.; Rapaić, M.R.; Jeličić, Z.D.; Lino, P.; Maione, G. Complex-order models: A system identification point of view. *Appl. Sci.* **2022**, *12*, 4768. [CrossRef]
21. Tepljakov, A.; Petlenkov, E.; Belikov, J. FOMCON: A MATLAB toolbox for fractional-order system identification and control. *Int. J. Microelectron. Comput. Sci.* **2011**, *2*, 51–62.
22. Roslan, M.N.B.; Bingi, K.; Devan, P.A.M.; Ibrahim, R. Design and development of complex-order PI–PD controllers. *Appl. Syst. Innov.* **2024**, *7*, 33. [CrossRef]
23. Shah, P.; Sekhar, R.; Iswanto, I.; Shah, M. Complex-order $PI^{a+jb}D^{c+jd}$ controller design for a factional order DC motor system. *Adv. Sci. Technol. Eng. Syst. J.* **2021**, *6*, 541–551. [CrossRef]
24. Abdulwahhab, O. Design of a complex fractional order PID controller for a first-order plus time delay system. *ISA Trans.* **2020**, *99*, 154–158. [CrossRef] [PubMed]
25. Podlubny, I.; Petráš, I.; Vinagre, B.M.; O'Leary, P.; Dorčák, L. Analogue realizations of fractional-order controllers. *Nonlinear Dyn.* **2002**, *29*, 281–296. [CrossRef]
26. Matignon, D. Stability results for fractional differential equations with applications to control processing. In *Proceedings of the Computational Engineering in Systems Applications (CESA), Lille, France, 9–12 July 1996*; IEEE: New York, NY, USA, 1996; Volume 2, pp. 963–968.
27. Busłowicz, M.; Kaczorek, T. Simple conditions for practical stability of positive fractional discrete-time linear systems. *Int. J. Appl. Math. Comput. Sci.* **2009**, *19*, 263–269. [CrossRef]
28. Podlubny, I. *Fractional Differential Equations*; Academic Press: San Diego, CA, USA, 1998.
29. Merrikh-Bayat, F. Rules for selecting the parameters of Oustaloup recursive approximation for the simulation of linear feedback systems containing $PI^{\lambda}D^{\mu}$ controller. *Commun. Nonlinear Sci. Numer. Simul.* **2012**, *17*, 1852–1861. [CrossRef]
30. Krishna, B.T. Studies on fractional-order differentiators and integrators: A survey. *Signal Process.* **2011**, *91*, 386–426. [CrossRef]
31. Pachori, R.B. *Time-Frequency Analysis Techniques and Their Applications*; CRC Press: Boca Raton, FL, USA, 2023.
32. El-Khazali, R. Fractional-order LC αL filter-based grid-connected PV systems. In *Procceedings of the IEEE 62nd International Midwest Symposium on Circuits and Systems (MWSCAS), Dallas, TX, USA, 4–7 August 2019*; IEEE: New York, NY, USA, 2019; pp. 533–536. [CrossRef]
33. Batiha, I.M.; El-Khazali, R.; Ababneh, O.Y.; Ouannas, A.; Batyha, R.M.; Momani, S. Optimal design of $PI^{\rho}D^{\mu}$ controller for artificial ventilation systems for COVID-19 patients. *AIMS Math.* **2023**, *8*, 657–675. [CrossRef]
34. Freeborn, J.; Maundy, B.; Elwakil, A. Second-order approximation of the fractional Laplacian operator for equal-ripple response. In *Proceedings of the 53rd IEEE International Midwest Symposium on Circuits and Systems, Seattle, WA, USA, 1–4 August 2010*; IEEE: New York, NY, USA, 2010; pp. 1173–1176. [CrossRef]
35. El-Khazali, R. On the biquadratic approximation of fractional-order Laplacian operators. *Analog. Integr. Circuits Signal Process.* **2015**, *82*, 503–517. [CrossRef]
36. Colín-Cervantes, J.D.; Sanchez-Lopez, C.; Ochoa-Montiel, R.; Torres-Munoz, D.; Hernandez-Mejia, C.M.; Sánchez-Gaspariano, L.A.; González-Hernández, H.G. Rational approximations of arbitrary order: A survey. *Fractal Fract.* **2021**, *5*, 267. [CrossRef]
37. Zourmba, K.; Fischer, C.; Gambo, B.; Effa, J.Y.; Mohamadou, A. Fractional integrator circuit unit using Charef approximation method. *Int. J. Dyn. Control* **2020**, *8*, 943–951. [CrossRef]
38. Mitkowski, W.; Oprzędkiewicz, K. An estimation of accuracy of Charef approximation. In *Theoretical Developments and Applications of Non-Integer Order Systems: Proceedings of the 7th Conference on Non-Integer Order Calculus and Its Applications, Szczecin, Poland*; Springer: Cham, Switzerland, 2015; pp. 71–80. [CrossRef]

39. Oprzędkiewicz, K. Approximation method for a fractional-order transfer function with zero and pole. *Arch. Control Sci.* **2014**, *24*, 447–463. [CrossRef]
40. Deniz, F.N.; Alagoz, B.B.; Tan, N.; Atherton, D.P. An integer-order approximation method based on stability boundary locus for fractional-order derivative/integrator operators. *ISA Trans.* **2016**, *62*, 154–163. [CrossRef] [PubMed]
41. El-Khazali, R.; Tawalbeh, N. Realization of fractional-order capacitors and inductors. In Proceedings of the 5th Workshop Fractional Differentiation and Its Applications (FDA), Nanjing, China, 14–17 May 2012.
42. Chen, Y.Q. Step Response Invariant Discretization of Fractional Order Integrators/Differentiators. MATLAB Central File Exchange. 2026. Available online: https://www.mathworks.com/matlabcentral/fileexchange/21363-step-response-invariant-discretization-of-fractional-order-integrators-differentiators (accessed on 27 April 2026).
43. Chen, Y.Q. Impulse Response Invariant Discretization of Fractional Order Integrators/Differentiators. MATLAB Central File Exchange. 2026. Available online: https://www.mathworks.com/matlabcentral/fileexchange/21342-impulse-response-invariant-discretization-of-fractional-order-integrators-differentiators (accessed on 27 April 2026).
44. Wu, Z.; Chen, Y.Q.; Li, D. Impulse Response Invariant Discretization of Complex Fractional Order Integrator. *arXiv* **2019**, arXiv:1911.05835. [CrossRef]
45. De Keyser, R.; Muresan, C.I.; Ionescu, C.M. An efficient algorithm for low-order direct discrete-time implementation of fractional-order transfer functions. *ISA Trans.* **2018**, *74*, 229–238. [CrossRef]
46. Soloklo, H.N.; Bigdeli, N. Direct approximation of fractional-order systems as a reduced integer/fractional-order model by genetic algorithm. *Sadhana* **2020**, *45*, 277. [CrossRef]
47. Machado, J.A.T.; Galhano, A.M.; Oliveira, A.M.; Tar, J.K. Optimal approximation of fractional derivatives through discrete-time fractions using genetic algorithms. *Commun. Nonlinear Sci. Numer. Simul.* **2010**, *15*, 482–490. [CrossRef]
48. Das, S.; Majumder, B.; Pakhira, A.; Pan, I.; Das, S.; Gupta, A. Optimizing continued fraction expansion based IIR realization of fractional-order differ-integrators with genetic algorithm. In *Proceedings of the International Conference on Process Automation, Control and Computing, Coimbatore, India, 20–22 July 2011*; IEEE: New York, NY, USA, 2011; pp. 1–6.
49. Hartikainen, M.; Miettinen, K.; Wiecek, M. Constructing a Pareto front approximation for decision making. *Math. Methods Oper. Res.* **2011**, *73*, 209–234. [CrossRef]
50. Deb, K. *Multi-Objective Optimization Using Evolutionary Algorithms*; Wiley: New York, NY, USA, 2001.
51. Matignon, D. Stability properties for generalized fractional differential systems. *ESAIM Proc.* **1998**, *5*, 145–158. [CrossRef]
52. Ogata, K. *Modern Control Engineering*; Prentice Hall: Upper Saddle River, NJ, USA, 2010; Original published in Academic Press: San Diego, CA, USA, 1999.
53. Onyedi, T.; Tepljakov, A.; Petlenkov, E. FOMCONpy: Fractional-order modelling and control library for Python. In *Proceedings of the 43rd International Conference on Telecommunications and Signal Processing (TSP), Milan, Italy, 7–9 July 2020*; IEEE: New York, NY, USA, 2020; pp. 239–245. [CrossRef]
54. Chalupa, P.; Přikryl, J.; Novák, J. Modelling of twin rotor MIMO system. *Procedia Eng.* **2015**, *100*, 249–258. [CrossRef]

Disclaimer/Publisher's Note: The statements, opinions and data contained in all publications are solely those of the individual author(s) and contributor(s) and not of MDPI and/or the editor(s). MDPI and/or the editor(s) disclaim responsibility for any injury to people or property resulting from any ideas, methods, instructions or products referred to in the content.